Assessment of NASA SMAP Soil Moisture Products for Agricultural Regions in Central Mexico: An Analysis Based on the THEXMEX Dataset

Alejandro Monsiváis-Huertero, *Senior Member, IEEE*, Daniel Enrique Constantino-Recillas, *Student Member, IEEE*, Juan Carlos Hernández-Sánchez, *Student Member, IEEE*, Héctor Ernesto Huerta-Bátiz, *Student Member, IEEE*, Jasmeet Judge, *Senior Member, IEEE*, Pedro Alejandro López-Estrada, José Carlos Jiménez-Escalona, Eduardo Arizmendi-Vasconcelos, Marco Antonio García-Bernal, Cira Francisca Zambrano-Gallardo, Alejandra Aurelia López-Caloca, Enrique Zempoaltécatl-Ramirez, Iván Edmundo De la Rosa-Montero, Roberto Ivan Villalobos-Martínez, Ramón Sidonio Aparicio-García, Carlos Rodolfo Sánchez-Villanueva, Leonardo Arizmendi-Vasconcelos, Roberto Cotero-Manzo, *Student Member, IEEE*, Jaime Hugo Puebla-Lomas, and Víctor Manuel Saúce-Rangel

***Abstract*—Accurate knowledge of soil moisture (SM) is crucial in hydrological, micrometeorological, and agricultural applications; however, the SM estimation is particularly challenging in agricultural regions due to high spatial variability and dynamic vegetation conditions. The need for information about SM conditions is even more evident in developing countries with limited monitoring infrastructure. Satellite SM products are a useful tool as a proxy for SM conditions on the ground, but they need to be evaluated for specific regions. In this study, we assess the quality of the soil moisture active passive (SMAP) SM retrievals at 36, 9, and 3 km in an agricultural region in Central Mexico using *in situ* measurements during the Terrestrial Hydrology Experiments in Mexico 2018 and 2019. In addition, we provide insights into soil and vegetation parameters in the retrieval algorithms compared to those observed in the region. It was found that the SM spatial variability at the SMAP pixel grids was well represented by upscaled *in situ* SM measurements (SM_{up}) from five monitoring stations using the soil-weighted averaging and the Voronoï diagrams. Overall, the SMAP SM retrievals are highly correlated with SM_{up} at all scales, but they estimated wetter conditions and the average root-mean-square difference (RMSD) $> 0.045\ m^3/m^3$. The lowest RMSD was obtained for the SM product at 36 km, while the highest RMSD was found for the SM product at 3 km. In addition, the single-channel algorithm using H-polarization provided the lowest RMSD for the products at 36 and 9 km. The main sources of uncertainty in the region may arise from the higher clay fraction used in the SMAP retrieval algorithm, by 13% compared to that observed, and a nonrepresentative characterization of land cover heterogeneity for vegetation water content estimation. The incorporation of *in situ* values into an SM retrieval algorithm resulted in differences $<0.04\ m^3/m^3$ between SM estimates and *in situ* SM for the complete growing season. Particularly, the use of *in situ* information helped in improving SM estimation when optimizing V- and dual-polarization brightness temperature observations.**

***Index Terms*—Agricultural region, *L*-band passive microwave, Mexico, multiscale soil moisture (SM), soil moisture active passive (SMAP), terrestrial hydrology experiments in Mexico 2018 (THEXMEX-18), terrestrial hydrology experiments in Mexico 2019 (THEXMEX-19).**

Manuscript received October 3, 2021; revised January 31, 2022 and March 15, 2022; accepted March 18, 2022. Date of publication April 7, 2022; date of current version May 11, 2022. THEXMEXs and this work were supported in part by the Mexican Space Agency and the Consejo Nacional de Ciencia y Tecnología of Mexico under Grant AEM-2017-01-292774 and in part by the Instituto Politécnico Nacional of Mexico under Grant SIP-2018-1090 and Grant SIP-2020-1876. The work of Jasmeet Judge was supported by the NASA-Terrestrial Hydrology Program under Grant NNX16AQ24G. *(Corresponding author: Alejandro Monsiváis-Huertero.)*

Alejandro Monsiváis-Huertero, Héctor Ernesto Huerta-Bátiz, Marco Antonio García-Bernal, Cira Francisca Zambrano-Gallardo, Enrique Zempoaltécatl-Ramirez, Iván Edmundo De la Rosa-Montero, Roberto Ivan Villalobos-Martínez, Ramón Sidonio Aparicio-García, Carlos Rodolfo Sánchez-Villanueva, Leonardo Arizmendi-Vasconcelos, Roberto Cotero-Manzo, and Víctor Manuel Saúce-Rangel are with the Laboratorio de Investigación y Aplicaciones en Percepción Remota Espacial, ESIME Ticomán, Instituto Politécnico Nacional, Mexico City 7738, Mexico (e-mail: alejandromonsivais@yahoo.com; he.huerta.b@gmail.com; magarciabe@ipn.mx; czambranog@ipn.mx; ezempoaltecatl@ipn.mx; idelarosam1200@alumno.ipn.mx; roberto.villalobos.m@hotmail.com; rapariciog@ipn.mx; csanchezv_145@outlook.com; larizmendiv1300@alumno.ipn.mx; rcoterom2000@alumno.ipn.mx; vsaucer@ipn.mx).

Daniel Enrique Constantino-Recillas is with the ESIME Ticomán and ESIME Zacatenco, Instituto Politécnico Nacional, Mexico City 7738, Mexico, and also with Tecnológico Nacional de México-TESE, Mexico City 7738, Mexico (e-mail: dconstantinor1100@alumno.ipn.mx).

Juan Carlos Hernández-Sánchez is with the ESIME Ticomán and ESIME Zacatenco, Instituto Politécnico Nacional, Mexico City 7738, Mexico (e-mail: jchernandezsa@ipn.mx).

José Carlos Jiménez-Escalona and Eduardo Arizmendi-Vasconcelos are with the ESIME Ticomán, Instituto Politécnico Nacional, Mexico City 7738, Mexico, and also with Tecnológico Nacional de México-TESE, Mexico City 7738, Mexico (e-mail: jjimeneze@ipn.mx; earizmendiv1100@alumno.ipn.mx).

Jasmeet Judge is with the Center for Remote Sensing, Agricultural and Biological Engineering Department, The University of Florida, Gainesville, FL 32611 USA (e-mail: jasmeet@ufl.edu).

Alejandra Aurelia López-Caloca is with the Centro de Investigación en Ciencias de Información Geoespacial, Mexico City 14240, Mexico (e-mail: alopez@centrogeo.edu.mx).

Pedro Alejandro López-Estrada and Jaime Hugo Puebla-Lomas are with the ESCOM, Instituto Politécnico Nacional, Mexico City 7738, Mexico (e-mail: alopez.biesa@gmail.com; jpuebla@ipn.mx).

Digital Object Identifier 10.1109/JSTARS.2022.3165078

I. Introduction

ACCURATE knowledge of soil moisture (SM) is crucial in hydrology, micrometeorology, and agriculture for

estimating energy and moisture fluxes at the land surface. Estimates of SM can be significantly improved by using remotely sensed microwave observations at frequencies <10 GHz that are sensitive to SM changes in the upper few centimeters of the soil (near-surface SM) [1]–[3]. For SM studies, observations at *L*-band (1.2–1.4 GHz) are desirable due to larger penetration depth and system feasibility [2]. Currently, the National Aeronautics and Space Administration (NASA)—Soil Moisture Active/Passive (SMAP)—and the European Space Agency (ESA)—Soil Moisture and Ocean Salinity—missions [4], [5] include passive microwave sensors at *L*-band and provide global observations of brightness temperatures (T_B), with a repeat coverage of about three days and pixel sizes of 36 and 43 km, respectively. In addition to the passive observations at 36 km, the SMAP mission also provides high-resolution T_B observations at 3 and 9 km, using SMAP 36 km observations and 3 km observations at C-band from ESA Sentinel-1 [6], [7]. Since T_B observations are also sensitive to other land surface parameters, such as soil temperature (ST), surface roughness, and vegetation water content (VWC) [8], SM retrieval from T_B observations has been particularly challenging in agricultural regions due to high spatio-temporal variability of SM and dynamic vegetation conditions (e.g., [9]–[13]). In these regions, SMAP retrievals have shown a wide range of agreement with *in situ* SM with root-mean-square differences (RMSDs) between 0.02 and 0.05 m^3/m^3 (e.g., [12]–[18]). In many regions, particularly those not covered by the core validation sites, the SM retrievals have uncertainties >0.04 m^3/m^3 [12], [19]. For example, Colliander *et al.* [12] found errors >0.05 m^3/m^3 in croplands of the Pampean region in Argentina. These differences are mainly due to rapid changes in surface, diversity in climate, and agricultural practices that might be resulting in larger variations in the parameters compared to the global values used in SM retrieval algorithms. Identifying the parameters that are the main sources of uncertainties is critical for more accurate SM estimates covering a wider range of conditions worldwide.

Most of the studies evaluating SMAP SM products have been dedicated to the 36 km product [14] and very few have assessed products at finer resolutions (e.g., [19], [20]). Uncertainties in instrument noise, errors in the radiometric calibration, and assumptions in the retrieval model at different spatial scales result in systematic and random errors in the SM retrievals when compared to *in situ* SM measurements [21]. Studies addressing the effects of parametrization at different scales have pointed out the need to account for seasonal effects on retrievals when time-variant parameters are assumed constant or estimated using climatological information in the algorithms [20]. Colliander *et al.* [20] found that SM retrievals at airborne and satellite scales follow the trend of *in situ* SM, but the errors vary with scale and also over time. Studies have recommended accounting for multiscale effects of soil parameters [19], [20] and compensating for the rapidly changing vegetation, such as agricultural lands, at different scales over growing cycles [20]. The authors conclude the necessity of additional datasets to improve the understanding of the effects due to uncertainties in soil parameters and VWC on SMAP SM retrievals at agricultural lands and different spatial scales. However, such datasets need to fulfill minimum requirements to allow multiscale studies, such as the number of required locations (NRL) at different grid sizes.

Different efforts have been implemented to increase the number of reference locations and create global datasets, particularly in developing countries. In Latin America, the "Sistema Integral Regional de Información Satelital" is an international collaboration between the Inter-American Development Bank and the Space Agencies from Argentina, Bolivia, Chile, Ecuador, Mexico, Paraguay, Peru, and Uruguay [22] to provide satellite products over Latin America, including SMAP SM. However, very few agricultural validation sites in Latin America and the Caribbean have been included for validation [12], [23], [24], primarily because of the lack of mid- and long-term and/or reliable datasets of *in situ* SM. Due to the importance of agriculture in the region [25]–[27], more long-term datasets describing agricultural regions of Latin America and the Caribbean are needed to improve SM estimates in the region.

Existing datasets, including *in situ* SM for agricultural regions, in developing countries are based on sparse networks. Evaluation of the satellite SM products using these networks depends upon the upscaling method used [21], [28]. The challenge in the selection of the upscaling method arises from the heterogeneity in the spatial distribution of the SM as a result of soil texture, topography, vegetation, and climate [29]–[31]. Some of these features are static, while others vary spatially and/or temporally. Previous studies such as [19] have suggested the arithmetic method as representative enough of the SM conditions in an agricultural area. Bhuiyan *et al.* [30] concluded that the arithmetic mean and other upscaling methods obtain similar SM values for networks with a large number of SM stations; however, Crow *et al.* [32] recommended the utilization of other upscaling strategies different from the arithmetic mean for sparse networks to generate representative upscaled SM values accounting for heterogeneities of land cover, soil properties, and topography. Thus, a more detailed study is needed to select an approach specific to a region to upscale the field-scale values of SM to a reference satellite pixel.

As a response to this need, Terrestrial Hydrology Experiments in Mexico (THEXMEXs) have been conducted over different biomes, including agricultural lands, to monitor the dynamics of soil and vegetation [33]–[35]. During 2018 and 2019 (THEXMEX-18 and -19), an agricultural region was characterized by two complete growing seasons of corn in the region of Huamantla, Central Mexico. This two-season dataset included intensive ground sampling to characterize soil and vegetation and is used to assess the SMAP SM products at different spatial resolutions. In this study, we aim to understand the quality of the SMAP SM retrievals in Central Mexico and provide insights into parameters used in the retrieval algorithm. The specific objectives of this study are to: 1) compare different methods of upscaling *in situ* SM at the SMAP grid scales, 2) assess SMAP SM retrievals at spatial scales of 36, 9, and 3 km with *in situ* SM over different growing seasons, and 3) provide insights into the effects of the parameter uncertainty during the growing season using an SM retrieval algorithm based upon [36], focusing on the agricultural region in Central Mexico.

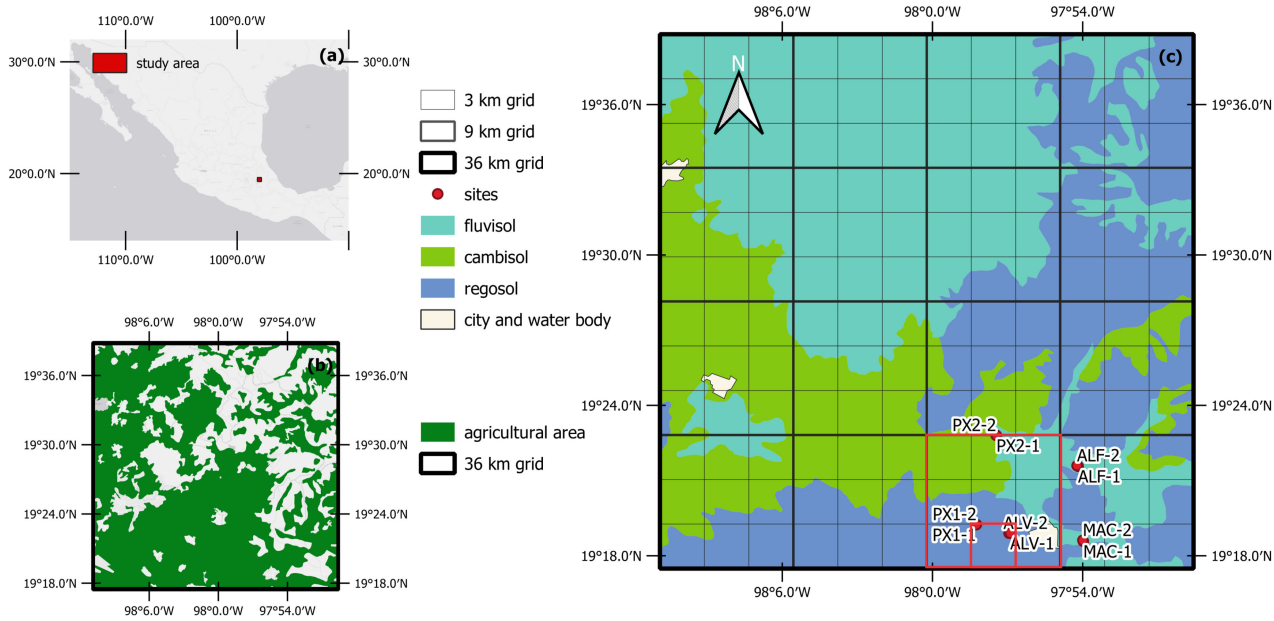

Fig. 1. (a) Geographical location of Huamantla, Tlaxcala, Mexico. (b) Agricultural land in the study area. (c) Soil types in the study area and grids at 3, 9, and 36 km based on the EASE Grid 2. The red boxes indicate the grids used for validation of the SMAP SM products at 9 and 3 km.

TABLE I
SOIL PARAMETERS OBSERVED DURING THEXMEX-18 AND THEXMEX-19 AT THE SAMPLING SITES (SEE FIG. 1)

Site ID	Coordinates	Soil properties					Site ID	Coordinates	Soil properties				
		Depth (cm)	Sand (%)	Silt (%)	Clay (%)	Bulk density (g/cm^3)			Depth (cm)	Sand (%)	Silt (%)	Clay (%)	Bulk density (g/cm^3)
MAC-1	19°18'34" N 97°53' 58" W	2.5	37.50	39.12	23.38	1.22	MAC-2	19°18'36" N 97°53'59" W	2.5	37.69	47.75	14.56	1.23
		5	37.24	42.06	20.71	1.22			5	38.12	49.03	12.85	1.23
		10	36.90	42.86	20.24	1.30			10	38.09	48.46	13.45	1.29
		20	39.31	41.61	19.07	1.24			20	38.25	50.43	11.32	1.34
		30	41.58	43.16	15.26	1.40			30	38.75	47.49	13.76	1.24
		60	43.06	45.05	11.89	1.22			60	43.94	46.88	9.17	1.29
		100	54.63	38.85	6.52	1.19			100	48.91	43.01	8.08	1.30
ALV-1	19°18'53" N 97°56'53" W	2.5	52.37	30.61	17.02	1.17	ALV-2	19°18'53" N 97°56'56" W	2.5	52.59	33.14	14.27	1.09
		5	52.98	30.37	16.65	1.08			5	51.64	36.25	12.11	1.06
		10	58.47	23.87	17.66	1.63			10	51.87	35.32	12.81	1.18
		20	55.10	26.25	18.65	1.16			20	55.40	34.13	10.47	1.15
		30	56.60	27.96	15.44	1.13			30	54.76	31.80	13.44	1.05
		60	59.00	24.77	16.24	0.94			60	57.80	26.88	15.32	0.90
ALF-1	19°21'34" N 97°54'11" W	2.5	73.13	13.60	13.27	1.03	ALF-2	19°21'36" N 97°54'13" W	2.5	63.10	19.53	17.37	1.08
		5	67.37	15.44	17.19	1.09			5	72.42	15.72	9.88	1.07
		10	68.21	16.01	14.51	1.15			10	73.75	15.65	10.60	1.30
		20	75.71	12.33	11.95	1.17			20	76.14	16.21	7.65	1.14
		30	75.88	13.84	10.28	1.05			30	79.69	13.72	6.58	1.19
		60	69.27	14.85	15.87	0.83			60	63.68	21.64	14.70	0.83
		100	39.61	26.67	33.72	0.92			100	47.43	21.81	30.77	0.92
PX1-1	19°19'26" N 97°58'15" W	2.5	46.80	29.01	24.19	1.13	PX1-2	19°19'27" N 97°58'15" W	2.5	48.10	34.58	17.32	1.22
		5	48.18	29.75	22.07	1.27			5	47.91	34.41	17.68	1.16
		10	52.87	24.84	22.29	1.16			10	46.96	38.16	14.88	1.27
		20	49.54	26.47	23.99	1.25			20	49.67	37.69	12.64	1.25
		30	52.63	26.84	20.53	1.12			30	49.52	35.96	14.51	1.28
		60	63.18	27.26	9.55	1.20			60	53.22	35.21	11.57	1.03
		100	37.31	44.09	18.60	1.15			100	48.53	27.00	24.47	1.15
PX2-1	19°23'07" N 97°56'57" W	2.5	22.29	53.13	24.58	1.14	PX2-2	19°23'12" N 97°56'56" W	2.5	35.37	46.89	17.73	1.22
		5	23.37	49.88	26.75	1.13			5	26.35	52.49	21.15	1.16
		10	27.96	49.55	22.49	1.24			10	29.05	52.25	18.71	1.40
		20	40.16	44.93	14.91	1.21			20	32.89	52.38	14.73	1.23
		30	47.79	39.04	13.17	1.18			30	37.68	45.00	17.33	1.27
		60	54.49	30.79	14.72	1.16			60	47.06	36.82	16.12	1.19
		100	44.17	40.58	15.24	1.11			100	28.19	49.47	22.34	1.08

II. TERRESTRIAL HYDROLOGY EXPERIMENTS IN MEXICO 2018 AND 2019

During 2018 and 2019 (THEXMEX-18 and -19), five corn fields within one 36 km SMAP pixel (see Fig. 1 and Table I) were characterized. The THEXMEX-18 and -19 were conducted from mid-April to mid-October in 2018 and from mid-March to early December in 2019, respectively. The protocols to measure the vegetation and soil parameters in the fields are based on [30], [37]–[39]. Fig. 2 presents the dates of data collection for soil and

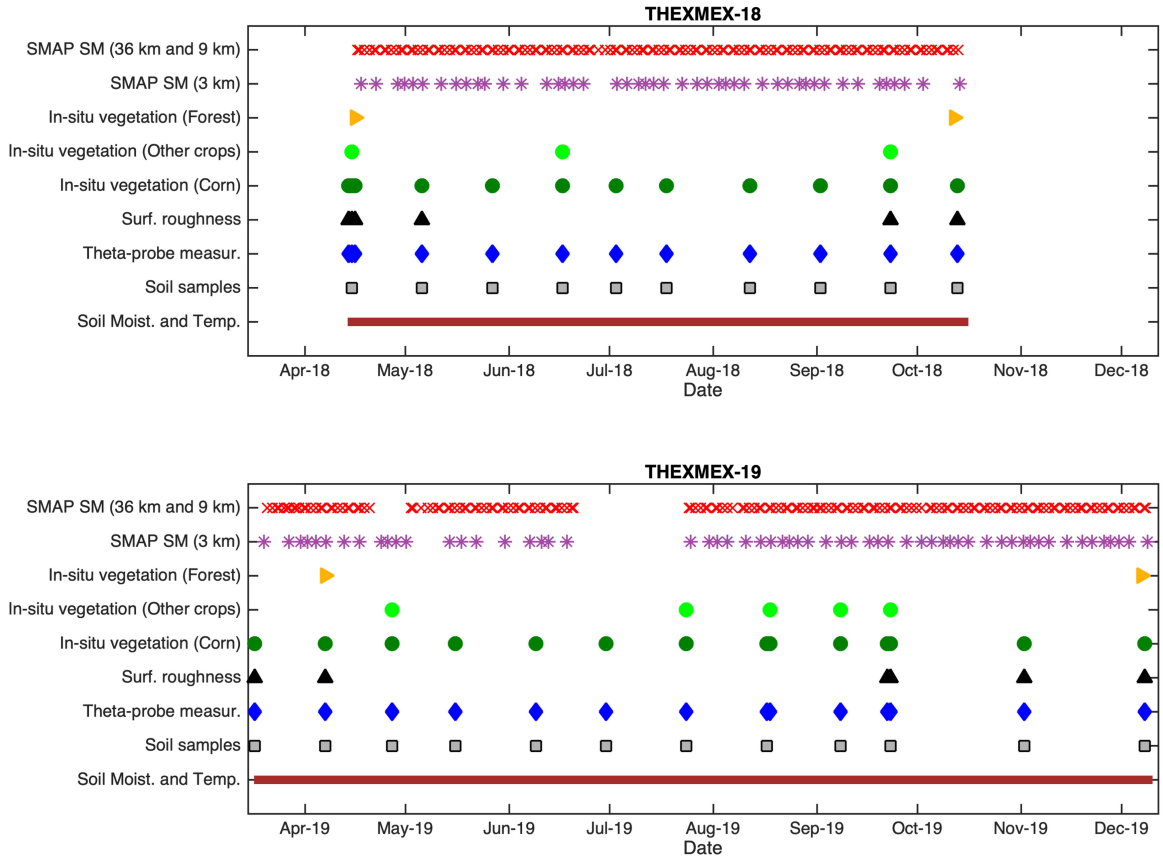

Fig. 2. Acquisition times for various observations during THEXMEX-18 and -19. For *in situ* vegetation observations, dark green and light green circles represent sampling dates for corn and other crops, respectively.

vegetation conditions. In this section, a detailed description of observations during the two field experiments used in the study is provided.

A. Site Description

The agricultural fields during both experiments are located in Huamantla, Central Mexico (19° 18′ 51.09″N; 97° 51′ 27.91″W) (see Fig. 1). Huamantla is a small city in Huamantla Municipality located in the eastern half of the Mexican state of Tlaxcala. The municipality's economy is still heavily dominated by agricultural activities, with almost a third of the workforce dedicated to crops and livestock. Over half of the municipality's territory is used for farming and grazing, but agriculture's role has been diminishing. The municipality has about 25 000 ha under cultivation with crops, such as corn, oat, alfalfa, beans, wheat, animal feed, and pumpkin, and the livestock activities, including the cattle for dairy, pigs, sheep, goats and domestic fowl [40]. The climate of Huamantla is characteristically temperate (subhumid). Rainfall occurs from May to October, ranging from 500 mm per year East to 800–1000 mm in the Southwest. Rainfall variations in the midsummer months can lead to extended droughts. Local farmers use the rainy season to cultivate the different crops. Average monthly temperatures fluctuate within a narrow range, with January being the coldest month (0–9 °C) and April or May generally the warmest (19–27 °C). Huamantla soils are generally sandy and highly drained, although some soils are gravelly or rocky. Depth varies from 10 cm in the Lithosols of the west and north-central regions to deep fluviols on the plains of Huamantla.

B. Soil Observations

SM was observed during the THEMEX-18 and -19 using a sparse temporary *in situ* network of SM sensors and manual SM measurements at specific locations within the five fields. Throughout the entire growing season of corn in the area, we operated a total of five automated data collection stations, one in each field. In addition to SM, these stations recorded ST every 20 min at depths of 2.5, 5, 10, 20, and 30 cm. SM was obtained from time-domain reflectometer (TDR) probes (Campbell Scientific CS-616) that were installed horizontally. This provided an integrated estimate for the SM profile for the surface SM. Each station included two independent sets of SM sensors at depths of 2.5 and 5 cm located at two opposite edges of the fields in order to have a better representation of the spatial distribution of the surface SM (0–5 cm). Precipitation gauges were installed to capture the high-intensity rainfall that is received during summer. Additionally, every three weeks, manual measurements of SM were conducted using Delta-T Theta probes to characterize the spatial variability of SM in the top 5 cm of the soil. In addition, soil samples at depths of 2.5, 5,

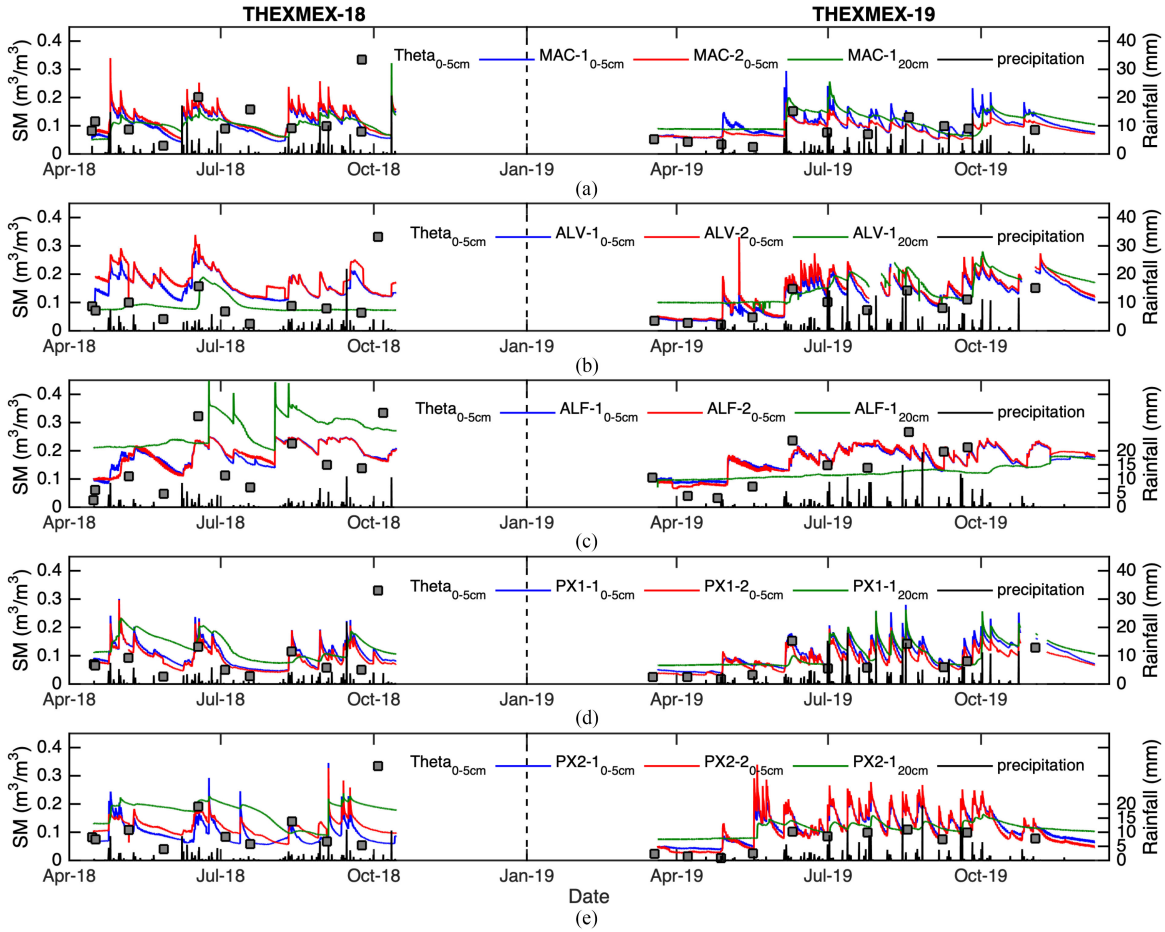

Fig. 3. *In situ* SM measurements and precipitations over the agricultural fields. (a) Sites MAC-1 and MAC-2. (b) Sites ALV-1 and ALV-2. (c) Sites ALF-1 and ALF-2. (d) Sites PX1-1 and PX1-2. (e) Sites PX2-1 and PX2-2.

10, 20, and 30 cm were collected at each field site to calibrate the SM sensors using a bulk density core (volume of 5 cm $\times$ 5 cm $\times$ 5 cm). The samples were placed in a plastic bag to minimize moisture loss, weighed wet, oven-dried for 24 h at 100 °C, and reweighed dry to obtain the gravimetric SM. These samples were also used to calculate the soil-specific bulk density and produce specific calibration equations for the TDRs and theta probes at each site. Calibration equations were developed independently for each site. In general, first-order polynomials were found to calibrate the Theta probes and second-order polynomials were needed to calibrate the TDR sensors. The RMSD between gravimetric SM measurements and the fitting curves was <0.03 (m^3/m^3) for both the Theta probes and the TDR sensors. These values of RMSD in the calibration of SM sensors are similar to those reported in the literature (e.g., [10], [11], [13], [30]). Fig. 3 shows the calibrated near-surface SM (0–5 cm) and 20 cm for each site using the different SM sensors; Fig. 4 shows the ST for all locations. It is observed that, during the study periods, the SM sensors were within their optimal temperature interval of operation.

Soil texture was also measured at each site using the sieving method with dried soil samples. Table I presents the percentage of sand, clay, silt, and bulk density for each site.

Surface soil roughness measurements of root-mean-square (RMS) height (h_{RMS}) and correlation length (cl) were also collected using a traditional grid board method [41] during the sampling dates for each site (see Fig. 2). The roughness measurements consisted of two components: a periodic component that is perpendicular to the plow lines and a random component that is parallel to the plow lines. During the measurements, leaf litter and wild grass were carefully removed. Ten 2-D surface profile pictures per site were taken using a 1.5-m-long grid board. The surface profile from each grid board was digitized individually to calculate h_{RMS} and cl [41]. Each soil roughness measurement was acquired by averaging the ten independent h_{RMS} and cl values.

C. Vegetation Observations

Vegetation properties for each corn field were measured at three sampling locations every three weeks during the complete growing season. A vegetation sampling consisted of measurements of height, width, biomass, leaf area index (LAI), geometric description of the plant, and VWC. The crop density was derived from the stand density and row spacing (76–80 cm) measured at the first sampling. In order to characterize the

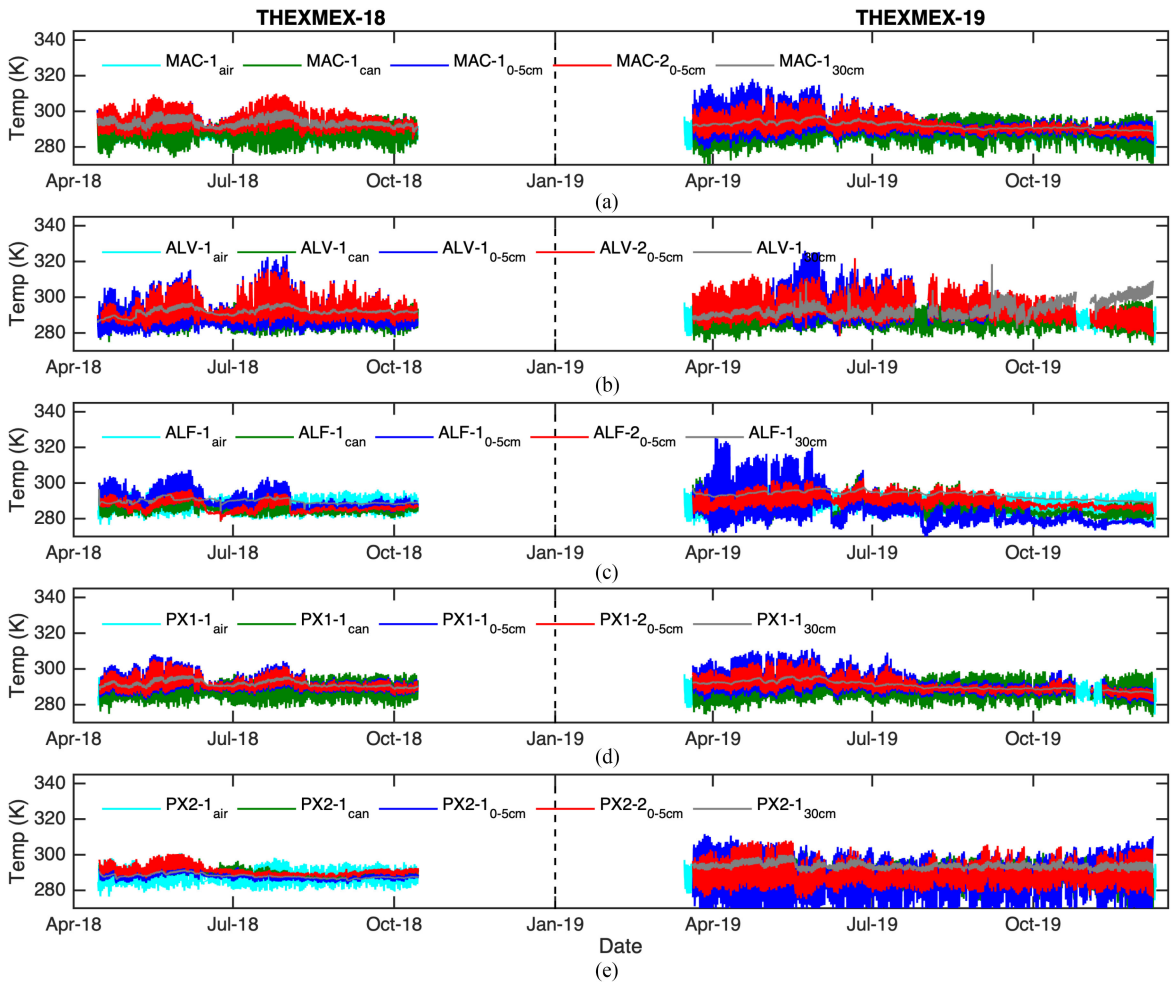

Fig. 4. Air temperature, canopy temperature, and *in situ* ST over the agricultural fields. (a) Sites MAC-1 and MAC-2. (b) Sites ALV-1 and ALV-2. (c) Sites ALF-1 and ALF-2. (d) Sites PX1-1 and PX1-2. (e) Sites PX2-1 and PX2-2.

vegetation biomass within each field, each sampling included one row of corn in the three sampling locations within a field. The sampling length started between two plants and ended at the next midpoint between plants was greater than or equal to 1 m away from the starting point, as mentioned in [30] and [39]. Two plants within this length were cut at the base, separated into leaves, stems, and ears, and weighed immediately. The samples were dried in the oven at 60 °C for one week and weighed. Destructive LAI was calculated using the equation presented in [42]. Fig. 5 shows the time series of VWC and crop height for each site.

In addition to the corn fields, VWCs from two fields of oats, two of pumpkins, one of alfalfa, one of wheat, and one of the vegetables in the study area were monitored. Because of the different growing seasons of these crops compared to corn, these sites were less intensively characterized and were measured three times for each experiment at different locations.

To provide best estimates of canopy conditions with the same temporal resolution as information from the soil stations, VWC and plant height at each sampling field were linearly interpolated in time between sampling rounds. For small numbers of sampling events per site, a piecewise linear fit is recommended as more adequate than nonlinear curve fitting [43].

D. Meteorological Conditions

Meteorological data were provided by the National Water Commission of Mexico (Comisión Nacional del Agua, CONAGUA) [44] and obtained from *in situ* stations located at the agricultural fields. The meteorological dataset includes information about accumulated precipitations and values of air temperatures (T_{air}) at temporal resolutions of 20 min and every hour, respectively. In addition, the precipitation was obtained from four different stations within a radius of 5 km surrounding the corn fields [45]. Figs. 3 and 4 show the precipitation and the soil and canopy temperatures, respectively, as collected by the meteorological stations for each corn field.

E. Land Cover Map

Land covers during the THEXMEX-18 and -19 were computed using information from the National Institute of Statistics

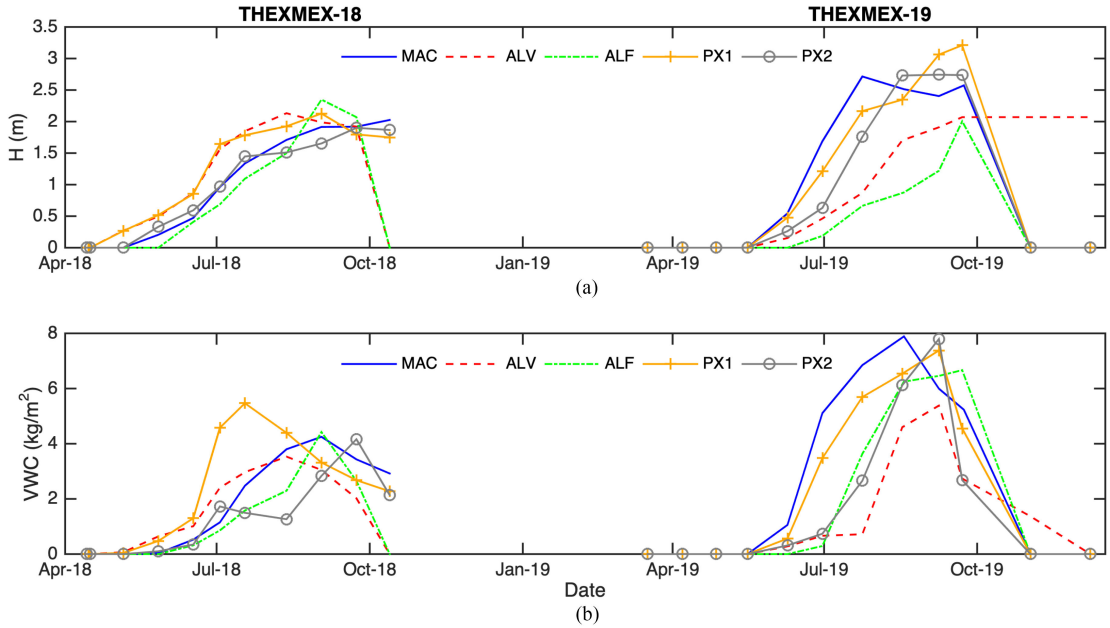

Fig. 5. Time series of the (a) plant height and (b) VWC over the agricultural fields.

and Geography of Mexico (INEGI) and a classification algorithm based on a genetic algorithm and a support vector machine (SVM) code to process Sentinel-2 images [46]. For both 2018 and 2019, the land cover was obtained from the classification algorithm at 10-m resolution using the location of about 50 agricultural fields to train and validate the final classification. The classification showed an accuracy higher than 70% at scales of 36, 9, and 3 km. Fig. 6 shows the land cover during the THEXMEX-18 and -19 and Table II lists the cover fractions for the main classes presented in the area at the different spatial scales.

III. SMAP Dataset

The passive SM product level-2 (L2SMP, version 7, R17030) has a grid resolution of 36 km, based on the equal-area scalable earth (EASE) grid, version 2 [36]. In this study, SM retrievals from three algorithms were used: V-polarization single-channel algorithm (SCA-V), H-polarization single-channel algorithm (SCA-H), and dual-channel algorithm (DCA). Among these three algorithms, the SCA-V algorithm is currently being used as the default option for the SM retrievals [14]; however, the SMAP SM product also includes the SM retrievals using the other two algorithms. In the two SCA algorithms, historical values of the normalized difference vegetation index (NDVI) product from the moderate-resolution imaging spectroradiometer (MODIS) is used to estimate VWC, while in the DCA, SM and the vegetation optical depth (τ) are retrieved simultaneously [47]. The enhanced 9-km SM product (L2SMPE, version 7, R17030) is based on the reconstructed SMAP T_B measurements at their native resolution of 36 km, using the Backus–Gilbert optimal interpolation method [36]. In addition, the high-resolution 3-km

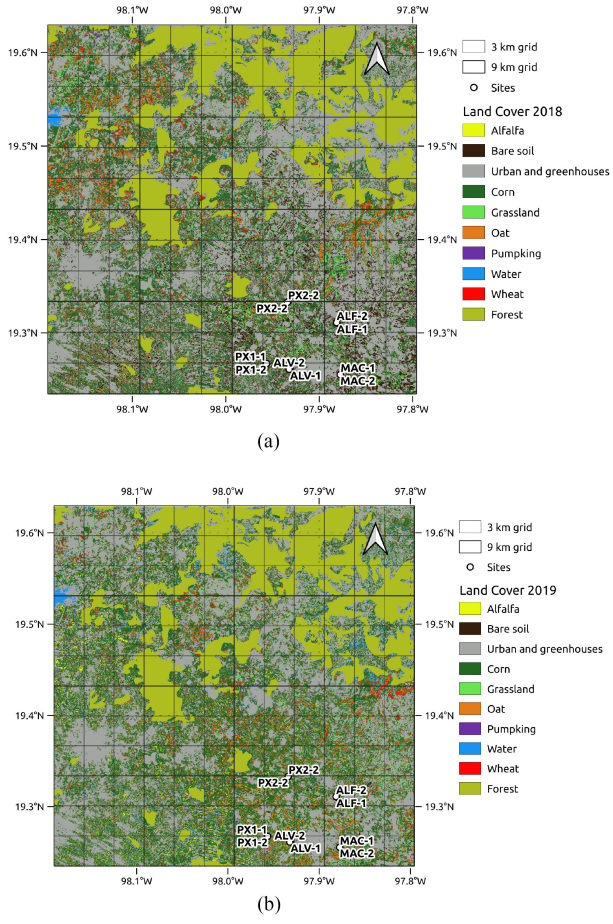

Fig. 6. Land covers observed at the grid resolutions of 36, 9, and 3 km during (a) THEXMEX-18 and (b) THEXMEX-19. The cover fractions are presented in Table II.

TABLE II
PERCENTAGE OF MAIN LAND COVERS DURING THEXMEX-18 AND THEXMEX-19 AT THE DIFFERENT SMAP GRIDS (SEE FIG. 6)

Class		36 km		9 km		3 km	
		2018	2019	2018	2019	2018	2019
Agricultural land	Corn	27.65	37.75	41.22	39.98	39.60	40.31
	Alfalfa	0.19	1.90	0.05	1.13	0.11	1.89
	Oat	4.91	6.28	3.01	16.88	1.88	11.50
	Pumpkin	1.84	1.73	2.67	2.67	2.45	1.52
	Wheat	2.04	0.98	2.01	0.55	2.65	0.44
	Bare soil	8.64	1.19	5.97	1.31	8.38	1.74
	Vegetables	4.74	2.88	6.88	5.14	3.64	3.37
Water bodies		0.19	1.55	0.00	0.00	0.00	0.10
Forest		17.95	17.95	0.00	0.00	0.00	0.00
Urban and greenhouse areas		31.84	27.79	38.19	32.35	41.28	39.14

product (L2SMAPS, version 3, R17030) was also used in this study. The product is based on merging SMAP *L*-band radiometer and Sentinel-1A/1B C-band radar data [7] and is available every 6–12 days.

During THEXMEX-18 and -19, 720 SM retrievals from the L2SMP, L2SMPE, and L2SMAPS products were obtained. No retrievals were available from 19 June to 23 July, 2019 due to SMAP's operation in safe mode.

IV. METHODOLOGY

A. Upscaling SM Methods

In this study, four upscaling approaches are implemented to obtain *in situ* SM at 36, 9, and 3 km. The performance of the upscaling methods is evaluated based on their representativeness errors, defined as the deviations of the upscaled SM from the *in situ* SM variations [21] and can be evaluated using second-order statistical moments, such as standard deviation and the coefficient of variation (CV) [28], [31]. The standard deviation also allows us to determine the optimal NRL to estimate the mean value of SM within an area with a prescribed absolute error and an established level of confidence. In the following sections, we briefly describe the upscaling methods and the statistics used to assess their performance.

1) Arithmetic Mean: The mean (SM_A) and the standard deviation (σ_A) at time t are given by

$$\mathrm{SM}_{A,t} = \frac{1}{N}\sum_{i=1}^{N}\mathrm{SM}_{i,t}$$

$$\sigma_{A,t} = \sqrt{\frac{1}{N}\sum_{i=1}^{N}(\mathrm{SM}_{i,t} - \mathrm{SM}_{A,t})^2} \tag{1}$$

where SM_i represents the surface SM value at the ith location and N indicates the number of locations. The resulting SM value is the upscaled surface SM within the satellite pixel. In this approach, arithmetic mean was calculated considering all the stations [48].

2) Soil-Weighted Average: The upscaling soil-weighted approach includes soil polygon aggregation based on soil texture information and then computation of the percent area within the SMAP footprint for each of the soil textures. The soil textures are aggregated into three categories: eutric cambisol, eutric fluvisol, and eutric regosol [see Fig. 1(c)]. *In situ* stations are categorized and clustered based on the soil textures of their locations. Based on the percent area of each of the soil texture classes, *in situ* surface SM values for each of the clusters are weighted on the percent area of the cluster within the SMAP pixel. The weight for each soil texture class (w_i) is obtained by

$$w_i = \frac{a_i}{A} \qquad \sum_{i=1}^{M} w_i = 1 \tag{2}$$

where a_i is the area of the ith class of soil texture, A represents the total area of the SMAP pixel, and M indicates the number of soil texture classes. The following equations are used to determine the upscaled *in situ* surface SM (SM_S) and its associated standard deviation (σ_S) at time t

$$\mathrm{SM}_{S,t} = \sum_{i=1}^{M} w_i \overline{\mathrm{SM}_{i,t}}$$

$$\sigma_{S,t} = \sqrt{\sum_{i=1}^{M} w_i \left(\overline{\mathrm{SM}_{i,t}} - \mathrm{SM}_{S,t}\right)^2} \tag{3}$$

where $\overline{\mathrm{SM}_i}$ represents the averaged surface SM of all stations located in the ith class of soil texture. It is noted that this is the default approach implemented by the SMAP team to upscale SM [12]. To develop the soil-weighted scaling approach, each *in situ* surface SM value is identified based on its corresponding soil texture. Then, soil texture data are intersected to the SMAP pixel, and percent area statistics are derived for each of the soil texture types [12].

3) Voronoï Diagram: A Voronoï diagram approach [49] is also used as an upscaling function and applied to the *in situ* surface SM information collected during the field campaigns, similar to previous works [30], [31], [34]. Input parameters used to generate the Voronoï diagram include the bounding area of the SMAP pixel and the geographical location of the *in situ* stations. The Voronoï diagram partitions the SMAP pixel into convex polygons (Thiessen polygons) based on the Euclidean distance between the measurement points [see Fig. 7(a)]. An area-based weighting function is then applied to the surface SM value measured by the *in situ* stations. The weight for each station is obtained by

$$w_i = \frac{b_i}{A} \qquad \sum_{i=1}^{N} w_i = 1 \tag{4}$$

where b_i is the area of the ith polygon, A represents the total area of the SMAP pixel, and N indicates the number of *in situ* SM stations. The upscaled *in situ* surface SM based on the Voronoï diagram (SM_V) and the standard deviation (σ_V) at time t are

$$\mathrm{SM}_{V,t} = \sum_{i=1}^{N} w_i \mathrm{SM}_{i,t}$$

$$\sigma_{V,t} = \sqrt{\sum_{i=1}^{N} w_i \left(\mathrm{SM}_{i,t} - \mathrm{SM}_{V,t}\right)^2}. \tag{5}$$

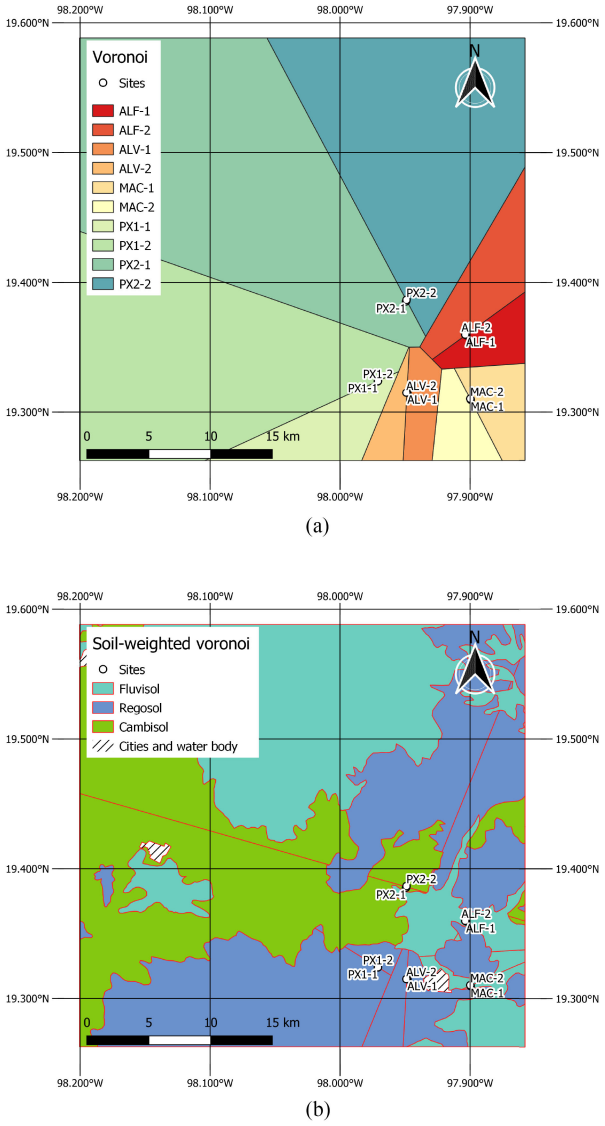

Fig. 7. Voronoï diagrams used for weighting the *in situ* SM measurements at 36 km grid for (a) Voronoï scaling method and (b) soil-weighted Voronoï scaling method.

4) Soil-Weighted Voronoï Diagram: The soil-weighted Voronoï diagram upscaling uses the intersection of the generalized soil texture information and the Voronoï diagram created from the *in situ* stations [see Figs. 1(c) and 7(a)]. The contribution of each *in situ* station to the upscaled surface SM was weighted by the area fraction defined by the intersection of the Thiessen polygons and the soil texture map [see Fig. 7(c)]. For this approach, the weights (w_{ij}) are given by

$$w_{ij} = \frac{c_{ij}}{A_j} \qquad A = \sum_{j=1}^{M} A_j \qquad \sum_{j=1}^{M}\sum_{i=1}^{L} w_{ij} = 1 \tag{6}$$

where c_{ij} indicates the area of the ith polygon located within the jth soil texture class, A_j is the total area covered by the jth soil texture class, L is the total number of *in situ* stations located within the jth soil texture class, and M represents the number of soil texture classes. The upscaled *in situ* surface SM based on the soil-weighted Voronoï diagram (SM_{SV}) and the standard deviation (σ_{SV}) at time t are

$$\mathrm{SM}_{SV,t} = \sum_{j=1}^{M}\sum_{i=1}^{L} w_{ij}\mathrm{SM}_{ij,t}$$

$$\sigma_{SV,t} = \sqrt{\sum_{j=1}^{M}\sum_{i=1}^{L} w_{ij}(\mathrm{SM}_{ij,t} - \mathrm{SM}_{SV,t})^2} \tag{7}$$

5) Statistical Assessment: The relationship between the standard deviation (σ) and the CV with the upscaled SM from each upscaling method is investigated. The CV in space at time t is calculated as [28]

$$\mathrm{CV}_t = \frac{\sigma_t}{\mathrm{SM}_t} \tag{8}$$

with σ_t and SM_t being the standard deviation and the upscaled SM, respectively, for each method described above.

The standard deviation and the CV can be used to estimate the optimal number of *in situ* SM stations as a function of the different SMAP scales. These relationships allow the characterization of the SM variability and, hence, to address the assessment of the NRL to estimate the scaled value of SM at the SMAP scale with a prescribed absolute error [21], [28], [31]. The NRL for a given time is determined by the following equation [28]:

$$\mathrm{NRL}_t = \left(t_{1-\alpha/2,\mathrm{df}}\frac{\sigma_t}{\mathrm{AE}}\right)^2 \tag{9}$$

where $t_{1-\frac{\alpha}{2},df}$ is the inverse Student's t-distribution at the confidence interval $\alpha/2$ and with (NRL $-$ 1) degrees of freedom (df) and AE is the absolute error expressed in ($\mathrm{m}^3/\mathrm{m}^3$). Given that the NRL is unknown and the degree of freedom as well, (9) is iteratively solved for NRL $= \{1, 2, ..., N\}$, with N being the number of *in situ* locations. The iterative process is conducted until the difference in the optimal number of stations is less than one station; this is until $|\mathrm{NRL}_k - \mathrm{NRL}_{k-1}| < 1$, with k representing the degree of freedom. In this study, we select α = 95% and AE = 0.03 $\mathrm{m}^3/\mathrm{m}^3$ based on the requirement of the SMAP mission. We also consider that the SM stations are located independently and normally distributed as is commonly assumed [21], [31].

B. Assessment of SMAP SM

To assess the SMAP SM, we compare the SM products at every 6-AM and 6-PM passes with the upscaled *in situ* SM to quantify their differences for each spatial resolution. The performance of the SM estimates from SMAP is statistically evaluated by the Bias, the RMSD, the unbiased RMSD (ubRMSD), and the Pearson correlation coefficient (r), as defined in [21].

C. Upscaling of Effective ST and VWC

The effects of using climatologically based effective ST and VWC were analyzed by comparing the upscaled *in situ* measurements at 36, 9, and 3 km with those used in the SMAP algorithm. This comparison provided an understanding of the effects of quick changes within the growing season.

In the SMAP SM retrieval algorithms, the soil effective temperature T_{eff} is estimated as [36]

$$T_{\text{eff}} = K\left[T_{\text{soil2}} + C(T_{\text{soil1}} - T_{\text{soil2}})\right] \tag{10}$$

where $C = 0.246$ for 6-AM SM retrieval and 1.0 for 6-PM SM retrieval and $K = 1.007$ for agricultural lands. T_{soil1} refers to the average ST for the first soil layer (0–10 cm) and T_{soil2} refers to the average ST for the second soil layer (10–20 cm). The upscaled T_{eff} is obtained using the same upscaling SM method that represents the best spatial variability in the region.

The VWC is upscaled based on an aggregation method of VWC [43] using the cover fraction of each class according to the land cover map (see Fig. 6 and Table II) to obtain the best representativeness of the variability in vegetation conditions at SMAP scales. In this study, the upscaled VWC is obtained as

$$\text{VWC} = \sum_{i=1}^{N} f_i \overline{\text{VWC}_i} \tag{11}$$

where f_i indicates the cover fraction for the ith class, $\overline{\text{VWC}_i}$ is the mean VWC for each ith class, and N is the total number of classes. Since corn is the dominant crop in the study region, the vegetated period in the area is divided into three corn growth stages defined as bare soil or early season, midseason, and late season. Bare-soil condition is defined when most of the corn fields have no vegetation cover or the plant height is lower than 15 cm. The midseason is characterized by the maximum vegetation growth and includes tasselling and silking phases of the corn plant. The late season represents the period of ear formation and harvest. For the THEXMEX-18, most of the corn fields were under bare-soil conditions from April 14 to May 1, in midseason from May 1 to July 7, and in late season from July 7 to 14 October 14. During the THEXMEX-19, the bare-soil conditions were identified from March 17 to April 15 and from November 1 to early December after harvest, midseason covered from April 15 to July 7, and late season from July 7 to November 1.

D. SM Retrieval Algorithm

To provide insights into the impact of uncertainty in clay fraction, T_{eff}, VWC, and roughness on SM retrievals, values used in the SMAP SM retrieval algorithm at 9 km [36] were replaced by *in situ* measurements at 9 km. The SM retrievals were conducted for the agricultural area using TB observations at H ($T_{B,H}$) and V ($T_{B,V}$) polarizations from the SMAP L1C_TB_E product concurrent with THEXMEX-18 and -19 observations. The optimization to estimate SM was carried out using $T_{B,H}$ and $T_{B,V}$ independently for the SCA-H- and SCA-V, respectively, and simultaneously both $T_{B,H}$ and $T_{B,V}$ for the DCA. The convergence was reached when the difference between the estimated and observed $T_{B,p}$ was lower than 1 K, corresponding to the uncertainty in SMAP T_B observations. To quantify the impact of the uncertainty, different SM retrieval scenarios were implemented. For each scenario, SM was estimated after replacing one parameter value used in the SMAP SM retrieval algorithm by the corresponding *in situ* value. The difference between the SM estimates obtained from these scenarios and the SMAP SM estimates provides the impact of each variable.

The forward model for the SM retrievals followed the SMAP passive SM retrieval algorithm based on [36]

$$T_{Bp} = T_s e_p \exp(-\tau_p \sec\theta) + T_c(1-\omega_p) \times [1-\exp(-\tau_p \sec\theta)][1+r_p \exp(-\tau_p \sec\theta)] \tag{12}$$

with

$$r_p = [(1-Q)r_{0p} + Q r_{0q}]e^{h\cos^{n_p}(\theta)} \tag{13}$$

and [8]

$$h = \left(\frac{0.9437(h_{\text{RMS}} \times 1000)}{0.8865(h_{\text{RMS}} \times 1000) + 2.2913}\right)^6 \tag{14}$$

where the subscripts p and q are H or V polarization, $\text{e}_p = 1 - r_p$ is the soil emissivity, T_s and T_c are the soil and vegetation temperatures, τ_p is the nadir vegetation opacity, ω_p is the effective scattering albedo from vegetation, and r_p is the rough soil reflectivity. The r_p is a function of dielectric constant ϵ and is estimated using [50]. The r_{0p} and r_{0q} represent the smooth surface reflectivities at p and q polarizations, respectively.

Based on the SMAP SM retrieval algorithm, ω_p is set to 0.0538 for the single-polarization configuration and set to 0.0715 for the dual-polarization configuration. The parameter Q in (13) is assumed to be 0 for single-polarization configuration and $Q = 0.1771$ h for dual-polarization configuration [47]. The n_p is equal to 2. When using *in situ* temperature information, T_{eff} is obtained using (10). The τ_p was obtained using either the information provided by the SMAP SM products or the in situ VWC with $\tau_p = b \times \text{VWC}$, where b is an empirical factor depending upon vegetation type, polarization, and phenology [51], [52]. For this study, b was equal to 0.11 for croplands [36].

V. Results

A. Field Observations During THEXMEX-18 and -19

1) Meteorological Conditions: The growing season during THEXMEX-18 was atypically dry [35], [53] with average monthly precipitation of 78.5 mm, while the conditions were more typical during THEXMEX-19 with an average of 90.5 mm. Particularly, in July 2018, the precipitation was about 90 mm lower than typically observed in the region. In addition, the precipitation was more uniformly distributed in 2019, compared to the 2018 season [see Fig. 3(a)–(e)]. The dry conditions and heterogeneous pattern of precipitation in 2018 caused two month-long drought periods from May 10th to June 7th and from July 14th to August 9th.

The difference in the precipitation pattern during the THEXMEX-18 and -19 also impacted the values for air temperature [see Fig. 4(a)–(e)]. During the THEXMEX-18, the average monthly air temperature was 288 K; in contrast, it was 287 K in the THEXMEX-19.

2) Land Surface Conditions: Fig. 3(a)–(e) shows the time series of SM at 0–5 cm for the ten sites (see Table I) during the THEXMEX-18 and −19. The SM values from the Theta probes

and TDR observations at 0–5 cm match well with gravimetric measurements, having an RMSD <0.03 m^3/m^3 and a correlation coefficient >0.68 for all sites. This indicates the representativeness of both sensors to characterize the SM conditions at the field sites.

The soil conditions varied among the five field sites, as shown in Fig. 3(a)–(e). In general, drier conditions were observed for fluvisol soils with a texture classified as a sandy loam (sites MAC-1 and MAC-2), whereas wetter conditions were observed for regosol soils with a texture classified as silt loam (sites PX1-1, PX1-2, ALV-1, and ALV-2) (see Fig. 1 and Table I). This soil texture-based behavior was also found at the Carman site during the SMAP Validation Experiment in 2016 conducted in Manitoba, Canada (SMAPVEX16-MB) [30]. The site PX2-2 consistently showed the wettest conditions in the top 5 cm during both growing seasons, whereas the site MAC-1 showed the driest conditions with a mean difference of 0.01 m^3/m^3 for both years. The atypical distribution in the rainfall pattern during the THEXMEX-18 resulted in very low values of SM, particularly at MAC-1 and MAC-2, with near-surface SM reaching values as low as 0.04 m^3/m^3 in July 2018.

The average monthly ST was 291 K in the top 5 cm. In agreement with the rainfall pattern, during the THEXMEX-18, higher values of ST were recorded compared to THEXMEX-19. In general, the warmest location was PX2-1, and the coolest location was MAC-1, with a mean difference of 2.61 K between the two sites.

The periodic component of the surface roughness is largely dependent upon the agricultural practices in the region and showed less variation among the five sites compared to the random component that is largely dependent upon the soil type. The periodic component could be represented as a sinusoidal function with a period of 78 cm and an averaged amplitude between crest and trough of 13.5 cm. For the random component, h_{RMS} ranges from 0.6 to 1.7 cm and cl from 7.1 to 30.7 cm. These values of h_{RMS} were within the same order of magnitude as reported in the literature for corn (e.g., [54]–[56]). Fields with other crops, such as oat, wheat, alfalfa, and vegetables, in the region had only the random component with values of 1.1–1.23 cm in h_{RMS} and 18.6–22.2 cm in cl. In general, these fields presented lower uncertainty in cl compared to corn fields. The areas covered by forest presented a mean h_{RMS} of 1.46 cm and mean cl of 14.5 cm, similar to other forested areas such as [34].

The differences between the rainfall pattern during the two seasons of corn also resulted in variations in crop growth. As observed in Fig. 5, the drier season of 2018 resulted in smaller plants reaching a mean height of 2.1 m, whereas, during the wetter season, the plants reached a mean height of 2.6 m. The site ALF, with a hybrid corn cultivar, reached the maximum height of 2.4 m in 2018 among the sites. In the wet season of 2019, this site reached a height of 2.5 m. Overall, the maximum height of 3.2 m was obtained by the site PX1 with a creole corn cultivar.

The VWC was also impacted by the variations in the meteorological conditions. The drier conditions resulted in maximum values of VWC ranging between 3.53 and 5.47 kg/m^2 in the corn plant in 2018; in contrast, the wetter season produced maximum values of VWC between 5.38 and 7.89 kg/m^2 [see Fig. 5(c)]. During the drier season, the maximum value of VWC was found in PX1 and the minimum value in ALV, both having a creole cultivar. In the wetter season, the maximum VWC was found in MAC and the lowest VWC in ALV, also both using creole cultivars. Based on observations during the visit to the fields, it was found that although the creole plants had significantly more yellow leaves compared to the hybrid plants, the stems of both creole and hybrid cultivars kept enough amount of water to maintain the corn plants alive. The selection of the most adapted corn cultivar for this area is still a remaining question due to the erratic pattern of rainfalls. The range of values in VWC for corn collected during these experiments has also been reported in other areas with similar warm and wet conditions. For instance, Vermunt *et al.* [57] reported maximum values of about 4.5 kg/m^2 over warm conditions in Florida, USA, whereas Judge *et al.* [13] and Cosh *et al.* [39] reported maximum values of VWC higher than 6.5 kg/m^2 under wet conditions in Iowa, USA.

VWCs of other crops in the region were typically lower than the maximum VWC of corn. For example, the mean maximum values of VWC during both seasons were 0.53 kg/m^2 for alfalfa, 0.365 kg/m^2 for oat, 1.62 kg/m^2 for pumpkin, 0.125 kg/m^2 for wheat, and 0.35 kg/m^2 for other vegetables. In contrast, the average VWC in the forest of 17.4 kg/m^2 was higher than the VWC in crops in both seasons. All these values of VWC were also confirmed using concurrent NDVI information from Landsat.

B. *Upscaling* in Situ *SM to 36, 9, and 3 km Grids*

Table III presents the mean σ and mean CV for each of the four upscaling methods at the scales of 36, 9, and 3 km. In all upscaling methods, the mean σ is <0.040 m^3/m^3, with a difference <0.006 m^3/m^3 among the upscaled SM from each method. At all scales, the lowest mean σ and the lowest mean CV are obtained by Voronoï method. As the scale decreases from 36 to 3 km, and the land conditions become more homogeneous, the difference between the mean σ from the upscaling methods also reduces.

Fig. 8 shows the comparison of the upscaled SM using the four different upscaling methods at 36, 9, and 3 km during the growing seasons. In general, the upscaled SM from the Voronoï's method shows drier SM when compared to the other upscaling methods throughout the THEXMEX-18 and -19. The arithmetic, soil-weighted, and soil-weighted Voronoï methods provide upscaled SM with differences of 0.01–0.015m^3/m^3 among them. The highest mean difference of 0.015 m^3/m^3 is observed between the arithmetic mean and the Voronoï method, whereas the mean difference among the Voronoï, soil-weighted, and soil-weighted Voronoï methods is always <0.01 m^3/m^3 at all spatial scales. The upscaled SM at 36 km exhibits the highest temporal variability in all the upscaling methods similar to [28]. All upscaling methods are able to identify the dry and wet periods in the area (e.g., the two drought periods in 2018) (see Fig. 3). The upscaled SM during those two periods ranged

TABLE III
MEAN VALUES OF STANDARD DEVIATION (σ), CV, AND THE NRL FOR THE FOUR UPSCALING METHODS AT SPATIAL SCALES OF 36, 9, AND 3 KM

Method	36 km			9 km			3 km		
	σ (m^3/m^3)	CV	NRL	σ (m^3/m^3)	CV	NRL	σ (m^3/m^3)	CV	NRL
Arithmetic	0.040	0.319	6	0.032	0.256	5	0.029	0.247	5
Soil-weighted	0.040	0.314	7	0.029	0.235	4	0.029	0.227	4
Voronoï	0.035	0.234	4	0.028	0.227	4	0.027	0.219	4
Soil-weighted Voronoï	0.035	0.303	7	0.028	0.227	4	0.028	0.222	4

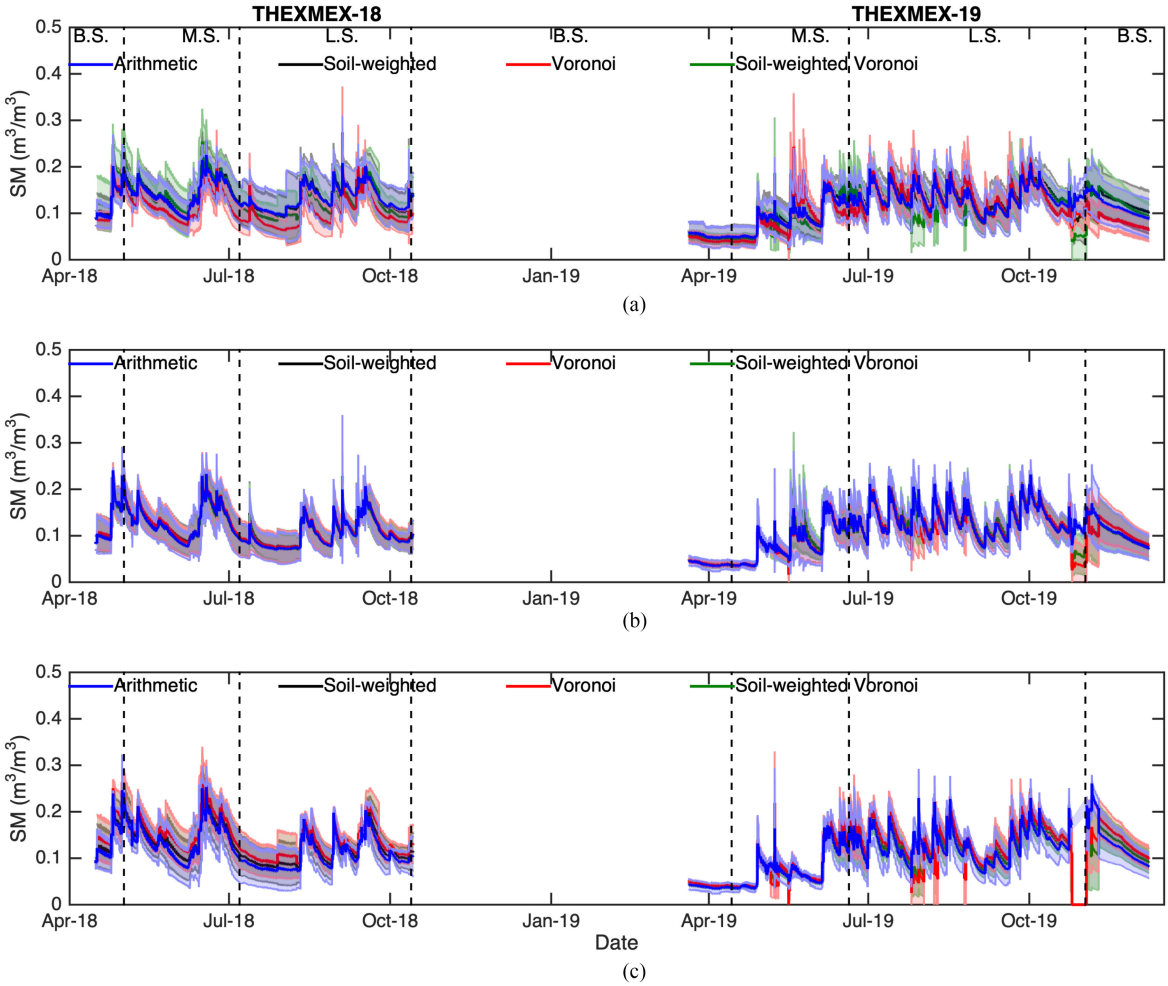

Fig. 8. Comparison between the upscaling SM methods for grids at (a) 36 km, (b) 9 km, and (c) 3 km. B.S. stands for bare-soil conditions, M.S. for mid-season, and L.S. for the late season of the corn growth stages.

between 0.07 and 0.095 m^3/m^3. These values are close to the wilting point of 0.05 m^3/m^3 for the soils in the region [58].

During 2019, when the rainfalls were more uniform throughout the season, the minimum values for the upscaled SM are >0.065 m^3/m^3 for all upscaling methods.

The CV is a statistical descriptor allowing the comparison of the variability of different samples even if characterized by different mean values, and, hence, to analyze the SM variability across different spatial scales. Fig. 9 compares the CV at scales of 36, 9, and 3 km. For all scales and all upscaling methods, the CV follows a negative exponential behavior as the SM increases similar to the results presented in [28] and [31]. The difference in CV among the upscaling methods is <0.12 for all values of SM at the three spatial scales. This result indicates that SM temporal variations are more significant than the spatial variations, hence confirming the importance of following the standardized criteria in monitoring SM, as those proposed in [21].

Table III and Fig. 9(b), (d), and (f) show the NRL for confidence of 95% at scales of 36, 9, and 3 km, respectively. At 36 km, the NRL varies from 3 to 9 for all upscaling methods; at 9 km, NRL ranges between 3 and 7; and at 3 km, it varies from 2 to 6. These values are within the range suggested in [12]

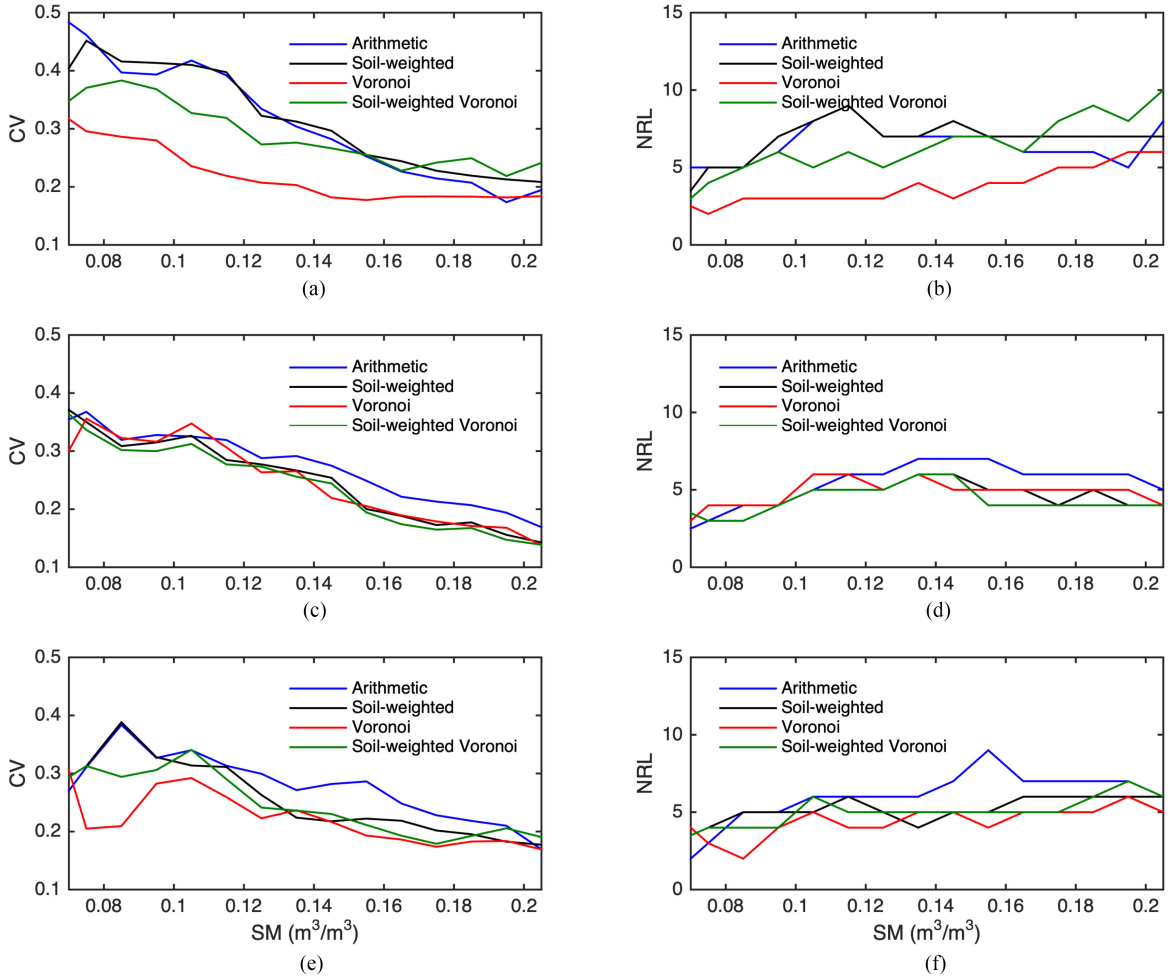

Fig. 9. CV and NRL at grids of (a)–(b) 36 km, (c)–(d) 9 km, and (e)–(f) 3 km.

to validate the SM product from SMAP. The lowest number of NRL at all spatial scales is obtained by the Voronoï method, while the highest number is shown by the arithmetic method.

For the agricultural region located in Central Mexico, Table III illustrates that the utilization of either Voronoï's technique or the soil-weighted method provides equivalent results in the representativeness of the SM values, even during extreme SM conditions, at the three spatial scales, similar to [12]. These upscaling methods require between 4 and 7 SM locations, depending upon the spatial scale, to be representative of SM conditions in the agricultural area with a confidence interval of 95% and an uncertainty lower than 0.03 m^3/m^3.

C. Evaluation of SMAP SM

The upscaled SM from the soil-weighted method and the Voronoï's diagrams were averaged to produce a representative upscaled *in situ* SM (SM_{up}) characterizing the agricultural region of Huamantla. Table IV presents the RMSD, the bias, the ubRMSD, and the correlation coefficient (r) between SM_{up} and the SMAP SM products. Overall, the SMAP SM retrievals were highly correlated with SM_{up}; however, the RMSD >0.04 m^3/m^3 at all scales. Similar RMSD values reported in Table IV have also been found in other agricultural areas, such as [13], [16], [17], [19], [30].

During both growing seasons, SMAP products at all scales estimate wetter conditions than SM_{up}, with a mean bias and ubRMSD of 0.07 m^3/m^3 and 0.05 m^3/m^3, respectively, over the region. The SCA-H algorithm provides the lowest bias and RMSD, while the DCA provides the highest bias and RMSD at 36 and 9 km (see Table IV). Figs. 10 and 11 show the time series of the three SMAP SM retrieval algorithms when compared to SM_{up} at 36 and 9 km, respectively. All SMAP retrieval algorithms produce SM following the same trend as SM_{up} measurements with $r > 0.56$. Particularly, the differences between SMAP SM and SM_{up} increase after rainfall events at 36 and 9 km grids. In addition, immediately after rainfall events, the SMAP estimated a higher dynamic range (0.13 m^3/m^3) compared to the dynamic range of 0.09 m^3/m^3 for SM_{up}. Wetter conditions throughout the growing seasons in the SMAP products suggest uncertainties in the soil and vegetation parameters used in the SMAP SM retrieval algorithm.

During bare-soil conditions, both the SCA algorithms show a low ubRMSD of 0.024 m^3/m^3 at 36 and 9 km. The ubRMSD

TABLE IV
RMSD, UBRMSD, AND CORRELATION COEFFICIENT (r) BETWEEN UPSCALED *IN SITU* SM (SM_{UP}) AND THE SMAP SM ESTIMATES FROM THE SMAP SM RETRIEVAL ALGORITHMS

Conditions	Grid (km)	N	SMAP algorithm	RMSD (m^3/m^3)	bias (m^3/m^3)	ubRMSD (m^3/m^3)	r
Overall	36	308	L2SMP SCA-H	0.045	0.016	0.042	0.73
			L2SMP SCA-V	0.086	0.075	0.043	0.73
			L2SMP DCA	0.123	0.110	0.055	0.72
	9	308	L2SMPE SCA-H	0.054	0.015	0.052	0.57
			L2SMPE SCA-V	0.090	0.074	0.053	0.56
			L2SMPE DCA	0.127	0.109	0.064	0.56
	3	104	L2SMAPS	0.087	0.063	0.060	0.41
Bare soil	36	68	L2SMP SCA-H	0.023	-0.009	0.021	0.87
			L2SMP SCA-V	0.055	0.051	0.021	0.89
			L2SMP DCA	0.082	0.075	0.033	0.87
	9	68	L2SMPE SCA-H	0.031	-0.016	0.027	0.79
			L2SMPE SCA-V	0.052	0.045	0.026	0.82
			L2SMPE DCA	0.078	0.070	0.036	0.81
	3	20	L2SMAPS	0.048	0.035	0.033	0.82
Mid season	36	91	L2SMP SCA-H	0.051	0.003	0.051	0.69
			L2SMP SCA-V	0.084	0.064	0.054	0.68
			L2SMP DCA	0.118	0.096	0.068	0.67
	9	91	L2SMPE SCA-H	0.060	0.005	0.060	0.55
			L2SMPE SCA-V	0.090	0.064	0.062	0.54
			L2SMPE DCA	0.122	0.097	0.074	0.54
	3	30	L2SMAPS	0.060	0.042	0.043	0.77
Late season	36	149	L2SMP SCA-H	0.048	0.036	0.032	0.58
			L2SMP SCA-V	0.099	0.093	0.034	0.55
			L2SMP DCA	0.141	0.135	0.041	0.54
	9	149	L2SMPE SCA-H	0.059	0.036	0.046	0.35
			L2SMPE SCA-V	0.104	0.092	0.047	0.30
			L2SMPE DCA	0.147	0.135	0.056	0.30
	3	54	L2SMAPS	0.099	0.074	0.065	0.09

increases to 0.044 m^3/m^3 during the vegetated period. However, the bias in the SM retrieved from the SCA-H algorithm changes from negative in bare soil into positive bias during the vegetated stages. In the late season, the SCA-H algorithm provides lower bias and RMSD than the SCA-V algorithm at both 36 and 9 km (see Table IV and Figs. 10 and 11). The difference between the performance of the two SCA algorithms during vegetated stages indicates that vegetation parameters used in the algorithm may not be representative of the region. As seen in Figs. 10 and 11, the SCA-H SM retrievals are closer to SM_{up} than the other two retrieval algorithms for all vegetated conditions for THEXMEX-18 and -19 at both 36 and 9 km.

At 3 km grid, the SMAP SM retrievals show a high bias and an RMSD of 0.063 m^3/m^3 and 0.087 m^3/m^3, respectively, with respect to the SM_{up} over the complete growing seasons (see Table IV), with a lower correlation coefficient of 0.41 than that at coarser resolutions. However, the correlations were high during bare-soil conditions, at >0.82, with a low bias and an RMSD of 0.035 m^3/m^3 and 0.048 m^3/m^3, respectively. Similar performance of the SMAP/Sentinel-1 retrieval algorithm was also reported in [7], [47] over other agricultural lands. Fig. 12 compares the time series of the SM_{up} and the SMAP SM retrievals at 3 km. During the vegetated period, the bias and RMSD gradually increased up to 0.063 m^3/m^3 and 0.087 m^3/m^3, respectively. As shown in Fig. 12, the difference between the SMAP SM retrievals and the SM_{up} has a dominant random component (ubRMSD) throughout the growing season for both the THEXMEX-18 and -19.

The SCA-H algorithm provides the closest estimates to the SM_{up} at 36 and 9 km compared to the other two retrieval algorithms; however, the high bias and RMSDs in the SM estimates from the SCA-V and DCA algorithms indicate the need to further examine the values used in the parameterization within the retrieval algorithm. Previous studies involving error characterization due to parameter calibration [8], [17], [20] suggest that the main sources of errors are due to uncertainty in soil texture, soil effective temperature, and τ that is directly related to VWC. As mentioned earlier, these parameters are derived from MODIS NDVI and global meteorological models [36]. These global parameters may not be representative at regional/local scales and could impact SM estimates, particularly for sites that have not been part of the calibration sites, such as the agricultural region in Huamantla, Mexico. In Section V-D, we analyze the impact of the values used in these variables on the SM estimates at 9 km over the agricultural region in Central Mexico.

D. Impact of the Parametrization in the SMAP SM Retrieval Algorithm on SM Estimates

Table V lists the statistics of the SM estimates when compared to the *in situ* SM after replacing the values used in the SMAP SM retrieval algorithm by *in situ* values. While the *in situ* clay content was about 18%, the SMAP retrieval algorithm uses a clay fraction of 31% (see Table I). This reduction of 13% in clay fraction resulted in an averaged decrease across the three retrieval algorithms of about 0.034 m^3/m^3 in bias and 0.023 m^3/m^3 in RMSD, getting closer to *in situ* SM. Significant improvements were observed for the SM estimates when using $T_{B,V}$ and dual-polarization configuration. Higher clay fraction results in lower soil permittivity according to the equations used

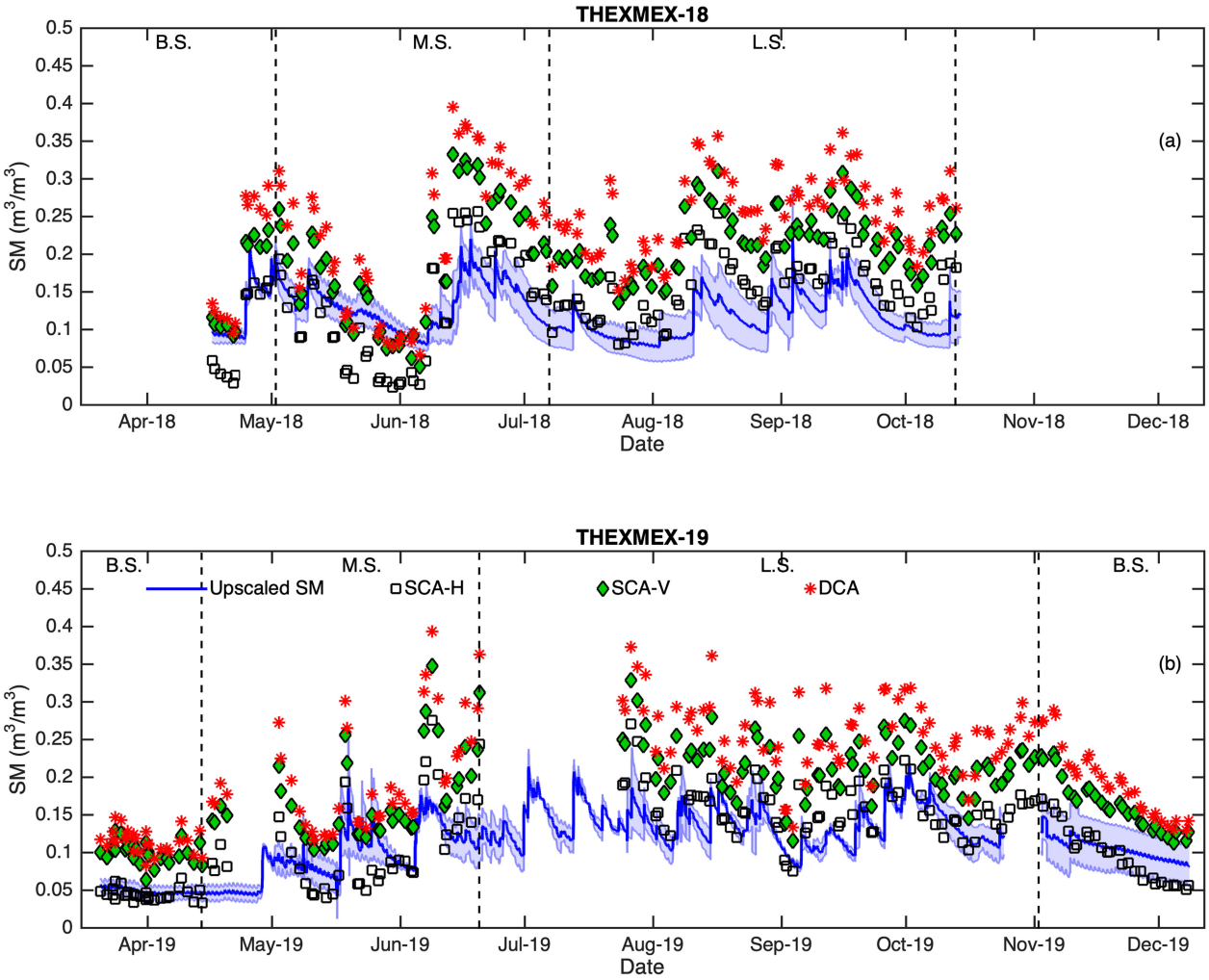

Fig. 10. Time series of the comparison between the SMAP SM retrieval algorithm using the SCA-H, SCA-V, and DCA options and *in situ* upscaled SM (SM_{up}) at 36 km grid. B.S. stands for bare-soil conditions, M.S. for mid-season, and L.S. for the late season of the corn growth stages.

in the SMAP algorithm [59] resulting in wetter SM compared to observed SM to compensate for the difference in soil texture. Singh *et al.* [19] also found a difference in the clay percentage considered in the SMAP SM and *in situ* information. They reported a clay value of 14% lower in the SMAP SM products than actual values over an agricultural area in India, estimating wetter conditions than *in situ* SM values. Soil texture descriptions of specific regions for satellite remote sensing can be improved using shapes developed by local governments. In Latin America, countries such as Mexico, Argentina, and Brazil have developed digital platforms to download freely edaphological maps of their territories (e.g., [60]–[62]).

When replacing the ST from the NASA Goddard Earth Observing System Model, Version 5 (GEOS-5) used to estimate T_{eff} in the SMAP algorithm by *in situ* ST measurements, the improvement in SM retrievals was marginal for all polarization configurations. It was found that an average seasonal difference of 3K resulted in an average reduction across the three retrieval algorithms of 0.002 m^3/m^3 in bias and 0.004 m^3/m^3 in SM retrievals when compared to *in situ* SM (see Table I). It is noted that for this agricultural region, there are no significant seasonal effects resulting in variations in the differences between T_{eff} and ST. Similar behavior was obtained by Walker *et al.* [16], reporting that the effective ST from SMAP SM products presents a difference of 0.6–1.2 K when compared to *in situ* information over an agricultural area in Iowa, USA.

Table V lists that the use of *in situ* VWC resulted in an averaged reduction of the bias greater than 0.039 m^3/m^3 and 0.037 m^3/m^3 in RMSD on the SM estimates at 9 km when compared to *in situ* SM, particularly for the optimization based on $T_{B,V}$ and dual-polarization configurations. The VWC in the SCA SMAP SM retrieval algorithm is obtained by using the climatology of NDVI from MODIS and shows the same values at scales of 36 and 9 km [see Fig. 13(a) and (b)]. The VWC used in the SMAP algorithm was found to be highly correlated with the *in situ* VWC; however, the VWC is higher by 1.7 kg/m^2 at 36 km, on average, than *in situ* values, while the VWC from the 9 km product is lower by 1.56 kg/m^2, on average. This indicates that although the climatological information adequately

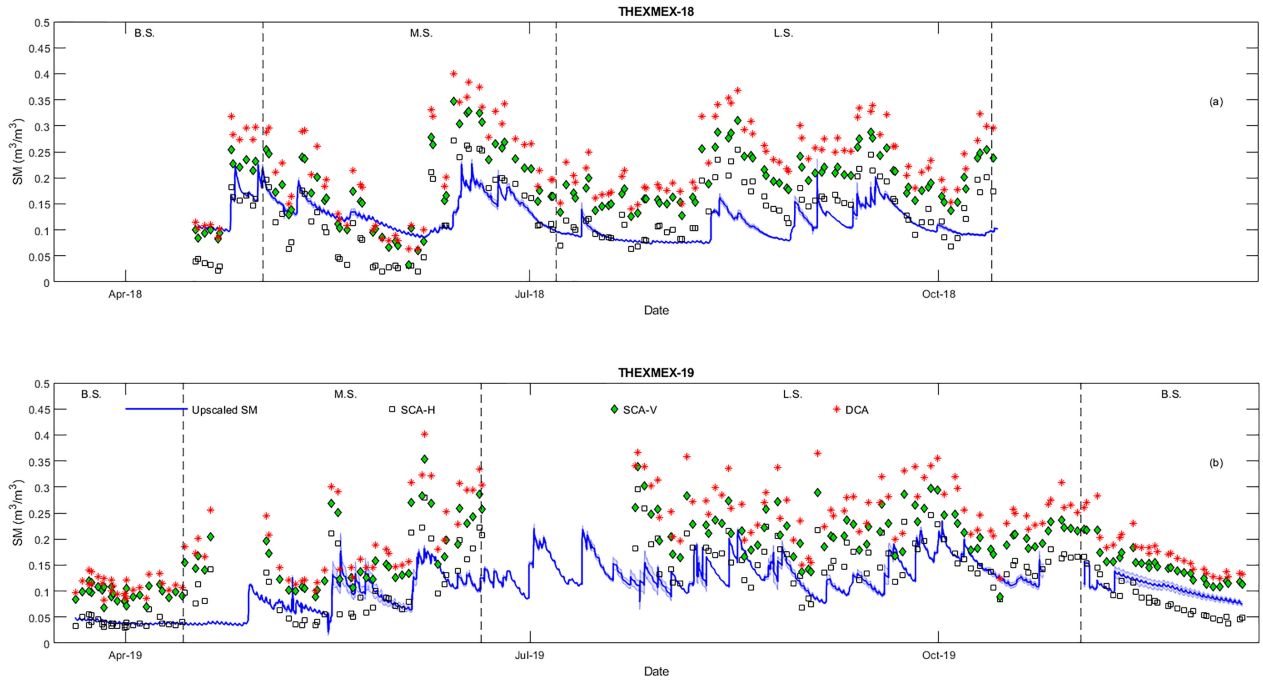

Fig. 11. Time series of the comparison between the SMAP SM retrieval algorithm using the SCA-H, SCA-V, and DCA options and *in situ* upscaled SM (SM_{up}) at 9 km grid. B.S. stands for bare-soil conditions, M.S. for mid-season, and L.S. for the late season of the corn growth stages.

TABLE V
RMSD, UBRMSD BETWEEN UPSCALED *IN SITU* SM (SM_{UP}) AND RETRIEVED SM USING *IN SITU* VWC, *IN SITU* CLAY FRACTION, AND SMAP T_B OBSERVATIONS AT 9 KM

Parameter value	$T_{B,H}$			$T_{B,V}$			$T_{B,H}$ and $T_{B,V}$		
	RMSD (m^3/m^3)	bias (m^3/m^3)	ubRMSD (m^3/m^3)	RMSD (m^3/m^3)	bias (m^3/m^3)	ubRMSD (m^3/m^3)	RMSD (m^3/m^3)	bias (m^3/m^3)	ubRMSD (m^3/m^3)
All SMAP values	0.054	0.015	0.052	0.090	0.074	0.053	0.127	0.109	0.064
in situ clay (%)	0.048	-0.009	0.047	0.062	0.038	0.049	0.090	0.068	0.058
in situ T_{eff} (K)	0.045	0.012	0.044	0.086	0.070	0.050	0.129	0.111	0.067
in situ VWC (kg/m^2)	0.050	-0.032	0.038	0.053	0.035	0.039	0.075	0.056	0.050
in situ h	0.071	0.051	0.050	0.111	0.098	0.051	0.078	0.060	0.050

[0]The label "all SMAP values" refers to SM retrievals obtained with values used in the SMAP algorithm.

represents the dynamics in the region, the VWC values may not be representative of the heterogeneity of the region. The difference between *in situ* VWC and VWC from 36 and 9 km has also been reported in previous works, such as [20]. In addition, during the early season, the SMAP products at 9 km classified the region as grassland instead of bare soil (see Fig. 6 and Table II). The estimation of actual conditions in VWC is not an easy task because of the heterogeneity in different areas and variability in actual vegetation conditions. Studies such as [13], [63], [64] have shown that it is possible to improve actual VWC estimates using information from microwave active sensors, such as Sentinel-1 and CONAE SAOCOM-A and -B and the future missions NASA/ISRO NISAR and ESA ROSE-L, and/or implementing constrained optimization algorithms to retrieve simultaneously SM and τ (accounting for VWC). These constraints need to be accounting for the land cover heterogeneity over the studied region. The characterization of these heterogeneous conditions requires reliable land cover maps at regional/local scales. A regional project called Latin American network for monitoring and studying of natural resources (SERENA) [65] was implemented using a large number of validation points to generate a land cover map including all countries within Latin America and the Caribbean for the year 2008 and can be used to include spatial variability information for this region.

The effect of the soil roughness was also analyzed in Table V. The relationship used to relate the empirical h parameter to *in situ* h_{RMS} was presented in (14). The value of the h parameter based on *in situ* information was 0.411, which is higher than the value used in the SCA option (0.12) and lower than that used in the DCA option (0.84). For the optimization of $T_{B,V}$ and $T_{B,H}$ (single-channel configurations), the SM retrievals marginally reduced the ubRMSD by 0.002 m^3/m^3 when compared to *in situ* SM. However, the bias and RMSD increased by 0.019 m^3/m^3 and 0.030 m^3/m^3, respectively. The most significant improvement was observed by the dual-polarization configuration with a reduction of 0.049 m^3/m^3 in both bias and RMSD. This confirms the polarization dependence of the h parameter for SM retrieval, similar to [8] and [13]. The SMAP SM retrieval algorithm relies

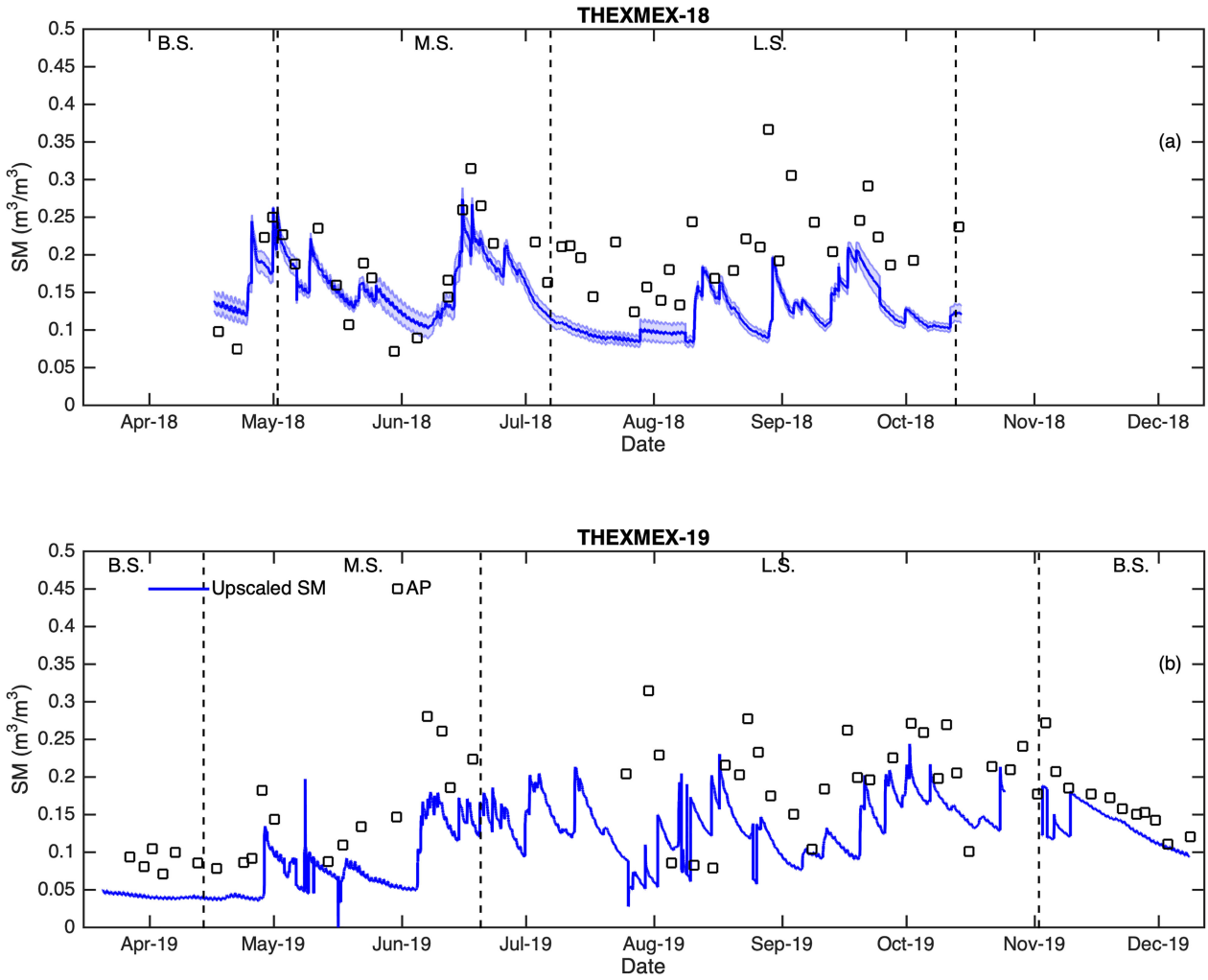

Fig. 12. Time series of the comparison between the SMAP SM retrieval algorithm and *in situ* upscaled SM (SM_{up}) at 3 km grid. B.S. stands for bare-soil conditions, M.S. for mid-season, and L.S. for the late season of the corn growth stages.

on a lookup table providing constant values of h based on the land cover types. Because of the high dependence of h upon other soil parameters [see (13)] and the complexity in finding a widely representative value of the roughness parameter h on SM retrievals at satellite scales, as highlighted in previous studies (e.g., [8], [66]), it is challenging to find an optimal global h value for most of the agricultural regions worldwide.

The use of *in situ* values in clay fraction and VWC in the SM retrieval algorithm shows the major improvement in the SM estimates over the agricultural region. Fig. 14 shows the time series of the SM estimates when using $T_{B,V}$ and dual-polarization observations from the L1C_TB_E product and incorporating simultaneously the *in situ* values in clay fraction and VWC during dry-down periods for THEXMEX-18 and -19. It is observed that the SM estimates when using these *in situ* values reduced their difference with *in situ* SM during the complete growing season for both years. During bare-soil conditions, the SM estimates showed mean differences of 0.011 m^3/m^3 and 0.026 $m^3/^3$ when optimizing $T_{B,V}$ and dual-polarization observations, respectively. During the vegetated period, the mean differences were 0.022 m^3/m^3 and 0.040 m^3/m^3 when optimizing $T_{B,V}$ and dual-polarization observations, respectively. This indicates that, although the differences increased during the vegetated periods, the SM estimates are within the SMAP requirements when incorporating *in situ* information within the retrieval process. When $T_{B,H}$ observations were optimized using *in situ* values of clay fraction and VWC, the results were similar to those observed from the SCA-H SMAP SM retrieval algorithm (see Table IV) with the RMSD and ubRMSD of SM estimates of 0.050 m^3/m^3 and 0.047 m^3/m^3, respectively.

VI. Conclusion

In this study, we provided insights into the difference and the seasonal trend of SM retrievals from the SMAP SM products at 36 km (L2SMP), 9 km (L2SMPE), and 3 km (L2SMAPS) in agricultural regions and analyzed the impact of uncertainty in soil and vegetation parameters on SM estimates at the three scales. It used high temporal resolution SM measurements up to 30 cm depth in the soil based on a sparse network and VWC

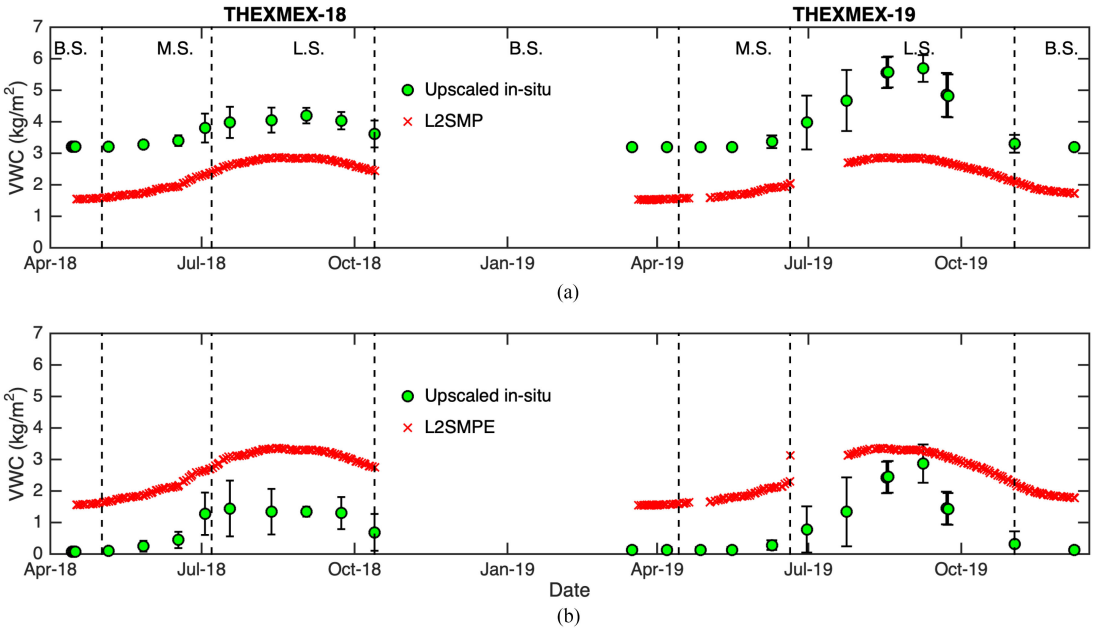

Fig. 13. Time series of the comparison between the VWC from the NASA SM products and *in situ* upscaled VWC at grids of (a) 36 km (SCA options) and (b) 9 km (SCA options). B.S. stands for bare-soil conditions, M.S. for mid-season, and L.S. for the late season of the corn growth stages.

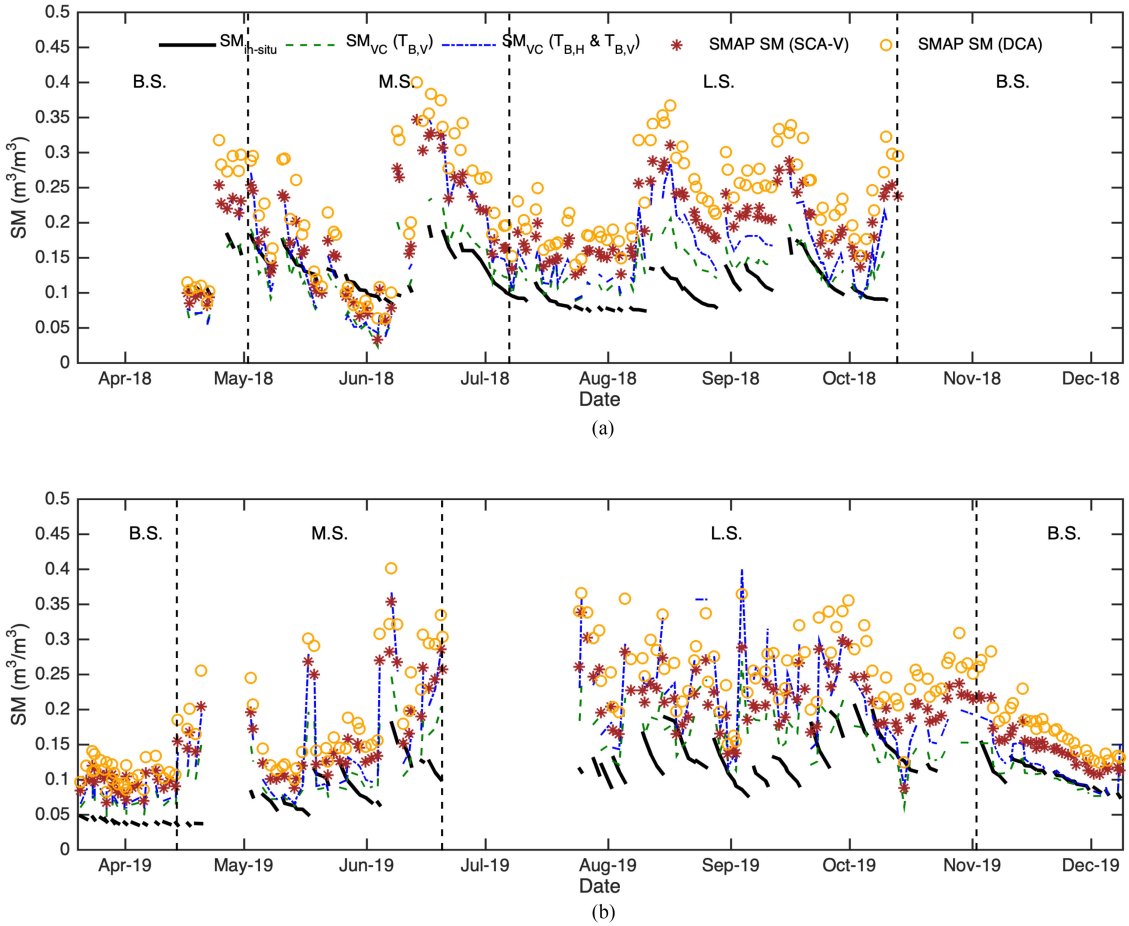

Fig. 14. Time series of the comparison between the upscaled *in situ* SM at 9 km ($SM_{in\ situ}$), retrieved SM using *in situ* values of VWC and clay (SM_{VC}) using SMAP $T_{B,V}$ and dual-polarization observations, and SMAP SM retrievals for (a) THEXMEX-18 and (b) THEXMEX-19. B.S. stands for bare-soil conditions, M.S. for mid-season, and L.S. for the late season of the corn growth stages.

information during two agricultural seasons from THEXMEX-18 and -19. Four SM upscaling methods were evaluated to understand the spatial representativeness of the *in situ* SM measurements at the SMAP scales: arithmetic mean, soil-weighted average, Voronoï diagram, and soil-weighted Voronoï diagram. Both the soil-weighted average and the Voronoï diagram obtained the best results with low standard deviation and high CV. In addition, it was found that the minimum NRL implemented during THEXMEX-18 and -19 to represent the variability of SM was fulfilled for these two upscaling methods at the three SMAP spatial scales with a confidence of 95% and an error of 0.03 m^3/m^3.

In general, the SMAP SM retrievals at 36, 9, and 3 km were well correlated with the upscaled SM; however, the SMAP products estimated wetter conditions and the RMSD $>$0.045 m^3/m^3 when compared with *in situ* SM. Among the different options in the SMAP SM retrieval algorithm, it was found that the single-channel algorithm based on H-polarization obtained the lowest bias and RMSD of 0.016 m^3/m^3 and 0.049 m^3/m^3, respectively, for the products at 36 and 9 km. For the 3-km SM product, the bias and RMSD were 0.063 m^3/m^3 and 0.087 m^3/m^3. The differences between the SMAP SM products and *in situ* SM were mainly due to uncertainties in soil and vegetation parameters, such as soil texture, effective ST, and VWC, that are impacting SM retrievals during the crop growing season in the agricultural area. It was found that the incorporation of available *in situ* information within the SM retrieval process reduced the differences of SM estimates when compared to *in situ* SM, particularly when V- and dual-polarization T_B observations were used in the optimization cost function. It was also observed that using simultaneously *in situ* values in clay fraction and VWC resulted in SM retrievals with mean differences lower than 0.04 m^3/m^3 when optimizing either single-channel or dual-channel T_B observations. The use of a local dataset validated by national institutions could correct the difference in soil texture information. Additional field experiments could help in improving relationships between statistical parameters characterizing the surface soil roughness and the empirical h parameter used in emission models. It was also observed that variations due to spatial heterogeneity in VWC changes at the SMAP pixel level were not properly characterized by the MODIS NDVI climatology. It is possible to improve actual VWC estimates using information from microwave active sensors, such as Sentinel-1 and SAOCOM-A and -B and the future missions NISAR and ROSE-L, and/or implementing constrained optimization algorithms, accounting for the land cover heterogeneity over the studied region, to retrieve simultaneously SM and τ.

The results of this study are particularly relevant to determining the applicability of SMAP SM retrievals in agricultural regions in Central America since the performance of the current SMAP baseline algorithm has been evaluated for the core validation sites that are mainly located in USA, Canada, Europe, and Australia—0.034. Overall, the results are encouraging of how the SMAP SM retrievals can be improved to enlarge their applicability over agricultural areas that are not included as validation core site. Improvement of some parameters such as VWC can be conducted by using active observations or derived information, such as the cross-polarization ratio as a proxy, as suggested in [13]. Utilizing current L- and C-band active missions, such as CONAE SAOCOM-A and -B and CSA Radarsat-2 and future SAR missions such as NASA/ISRO NISAR and ESA ROSE-L, is promising, particularly for regions lacking *in situ* vegetation information.

ACKNOWLEDGMENT

The authors would like to thank for the facilities provided by the farmers from the municipality of Huamantla, Tlaxcala, Mexico. They would also like to thank J. Mejía-González for her administrative assistance during the THEXMEX-18 and -19 and M.Sc., A. C. Torres-Gómez from the Centro de Investigación en Ciencias de Información Geoespacial, Mexico City, for her help in the implementation of the soil-sample protocol. They are also very thankful to Dr. P.-W. Liu from NASA's Goddard Space Flight Center and Science Systems and Applications, Inc., for his helpful comments about the main results found in this work. Data used in this research are available from the authors upon request.

REFERENCES

[1] H. McNairn and B. Brisco, "The application of C-band polarimetric SAR for agriculture: A review," *Can. J. Remote Sens.*, vol. 30, no. 3, pp. 525–542, 2004.

[2] F. Ulaby *et al.*, *Microwave Radar and Radiometric Remote Sensing*. Ann Arbor, MI, USA: Univ. Michigan Press, 2014.

[3] S. Steele-Dunne, H. McNairn, A. Monsivais-Huertero, J. Judge, P. Liu, and K. Papathanassiou, "Radar remote sensing of agricultural canopies: A review," *IEEE Trans. Geosci. Remote Sens.*, vol. 10, no. 5, pp. 2249–2273, May 2017.

[4] D. Entekhabi *et al.*, "The soil moisture active passive (SMAP) mission," *Proc. IEEE*, vol. 98, pp. 704–716, May 2010.

[5] Y. Kerr, P. Waldteufel, J. Wigneron, J. Martinuzzi, J. Font, and M. Berger, "Soil moisture retrieval from space: The soil moisture and ocean salinity (SMOS) mission," *IEEE Trans. Geosci. Remote Sens.*, vol. 39, no. 8, pp. 1729–1735, Aug. 2001.

[6] D. G. Long, M. J. Brodzik, and M. A. Hardman, "Enhanced-resolution SMAP brightness temperature image products," *IEEE Trans. Geosci. Remote Sens.*, vol. 57, no. 7, pp. 4151–4163, Jul. 2019.

[7] N. Das *et al.*, "The SMAP and copernicus sentinel 1A/B microwave active-passive high resolution surface soil moisture product," *Remote Sens. Environ.*, vol. 233, 2019, Art. no. 111380.

[8] J. Wigneron *et al.*, "Modelling the passive microwave signatures from land surfaces: A review of recent results and application to the l-band SMOS and SMAP soil moisture retrieval algorithms," *Remote Sens. Environ.*, vol. 192, pp. 238–262, 2017.

[9] K. Nagarajan and J. Judge, "Spatial scaling and variability of soil moisture over heterogeneous land cover and dynamic vegetation conditions," *IEEE Geosci. Remote Sens. Lett.*, vol. 10, no. 4, pp. 880–884, Jul. 2013.

[10] R. Magagi *et al.*, "Canadian experiment for soil moisture in 2010 (CanEx-SM10): Overview and preliminary results," *IEEE Trans. Geosci. Remote Sens.*, vol. 51, no. 1, pp. 347–363, Jan. 2013.

[11] H. McNairn *et al.*, "The soil moisture active passive validation experiment 2012 (SMAPVEX12): Prelaunch calibration and validation of the SMAP soil moisture algorithms," *IEEE Trans. Geosci. Remote Sens.*, vol. 53, no. 5, pp. 2784–2801, May 2015.

[12] A. Colliander *et al.*, "Validation of SMAP surface soil moisture products with core validation sites," *Remote Sens. Environ.*, vol. 191, pp. 215–231, 2017.

[13] J. Judge *et al.*, "Impact of vegetation water content information on SMAP soil moisture retrievals in agricultural regions: An analysis based on the SMAPVEX16-MicroWEX dataset," *Remote Sens. Environ.*, vol. 265, 2021, Art. no. 112623.

[14] S. Chan *et al.*, "Assessment of the SMAP passive soil moisture product," *IEEE Trans. Geosci. Remote Sens.*, vol. 54, no. 8, pp. 4994–5007, Aug. 2016.

[15] Y. Kerr *et al.*, "Overview of SMOS performance in terms of global soil moisture monitoring after six years in operation," *Remote Sens. Environ.*, vol. 180, pp. 40–63, 2016.

[16] V. Walker, B. Hornbuckle, M. Cosh, and J. Prueger, "Seasonal evaluation of SMAP soil moisture in the US corn belt," *Remote Sens.*, vol. 11, 2019, Art. no. 2488.

[17] X. Zheng *et al.*, "Performance of four passive microwave soil moisture products in maize cultivation areas of Northeast China," *IEEE J. Sel. Topics Appl. Earth Obs. Remote Sens.*, vol. 13, no. 1, pp. 2451–2460, May 2020.

[18] N. Ye *et al.*, "The soil moisture active passive experiments: Validation of the SMAP products in Australia," *IEEE Trans. Geosci. Remote Sens.*, vol. 59, no. 4, pp. 2922–2939, Apr. 2021.

[19] G. Singh *et al.*, "Validation of SMAP soil moisture products using ground-based observations for the paddy dominated tropical region of India," *IEEE Trans. Geosci. Remote Sens.*, vol. 57, no. 11, pp. 8479–8491, Nov. 2019.

[20] A. Colliander *et al.*, "Comparison of high-resolution airborne soil moisture retrievals to SMAP soil moisture during the SMAP validation experiment 2016 (SMAPVEX16)," *Remote Sens. Environ.*, vol. 227, no. 15, pp. 137–150, 2019.

[21] A. Gruber *et al.*, "Validation practices for satellite soil moisture retrievals: What are (the) errors?," *Remote Sens. Environ.*, vol. 244, 2020, Art. no. 111806.

[22] SIRIS, "Sistema regional integral regional de información satelital," 2021. [Online]. Available: http://www.sistemasiris.org

[23] M. Thibeault *et al.*, "Spatial and temporal analysis of the Monte Buey SAOCOM and SMAP core site," in *Proc. IEEE Int. Geosci. Remote Sens. Symp.*, 2015, vol. 1, pp. 969–971.

[24] P. Spennemann, M. Fernández-Long, N. Gattinoni, C. Cammalleri, and G. Naumann, "Soil moisture evaluation over the argentine pampas using models, satellite estimations and in-situ measurements," *J. Hydrol., Regional Stud.*, vol. 31, 2020, Art. no. 100723.

[25] PAHO FAO, WFP, and UNICEF, "Regional overview of food security in Latin America and the Caribbean: Towards healthier food environments that address all forms of malnutrition," *Food Agri. Org*., vol. 12, pp. 1–136, 2020.

[26] L. R. M. de Sousa, A. Saint-Ville, L. Samayoa-Figueroa, and H. Melgar-Quiñonez, "Changes in food security in Latin America from 2014 to 2017," *Food Secur.*, vol. 11, no. 3, pp. 503–513, 2019.

[27] J. M. Galeana-Pizaña, S. Couturier, and A. Monsivais-Huertero, "Assessing food security and environmental protection in Mexico with a GIS-based food environmental efficiency index," *Land Use Policy*, vol. 76, pp. 442–454, 2018.

[28] L. Brocca, T. Tullo, F. Melone, T. Moramarco, and R. Morbidelli, "Catchment scale soil moisture spatial-temporal variability," *J. Hydrol.*, vol. 422-423, pp. 63–75, 2012.

[29] N. Gaur and B. Mohanty, "Land-surface controls on near-surface soil moisture dynamics: Traversing remote sensing footprints," *Water Res.*, vol. 52, no. 8, pp. 740–752, 2016.

[30] H. Bhuiyan *et al.*, "Assessing SMAP soil moisture scaling and retrieval in the Carman (Canada) study site," *Vadose Zone J.*, vol. 17, no. 1, pp. 1–14, 2018.

[31] T. Caldwell *et al.*, "The Texas soil observation network: A comprehensive soil moisture dataset for remote sensing and land surface model validation," *Vadose Zone J.*, vol. 18, 2019, Art. no. 100034.

[32] W. T. Crow *et al.*, "Upscaling sparse ground-based soil moisture observations for the validation of coarse-resolution satellite soil moisture products," *Rev. Geophys.*, vol. 50, no. 2, pp. 1–20, 2012.

[33] A. Monsiváis-Huertero *et al.*, "The Thexmex-18 dataset: Understanding the soil and vegetation dynamics of agricultural fields in central Mexico from L-band SMAP observations," in *Proc. IEEE Int. Geosci. Remote Sens. Symp.*, 2019, pp. 6190–6193.

[34] A. Monsiváis-Huertero *et al.*, "Impact of temporal variations in vegetation optical depth and vegetation temperature on L-band passive soil moisture retrievals over a tropical forest using in-situ information," *Int. J. Remote Sens.*, vol. 41, no. 6, pp. 2098–2139, 2020.

[35] H. E. Huerta-Bátiz, D. E. Constantino-Recillas, A. Monsiváis-Huertero, J. C. Hernández-Sánchez, J. Judge, and R. S. Aparicio-Garcia, "Understanding root-zone soil moisture in agricultural regions of central Mexico using the ensemble Kalman filter, satellite-derived information, and the THEXMEX-18 dataset," *Int. J. Digit. Earth*, vol. 15, no. 1, pp. 52–78, 2022.

[36] P. O'Neill, S. Chan, E. Njoku, T. Jackson, and R. Bindlish, "Algorithm theoretical basis document level 2 and 3 soil moisture (Passive) data products, version D," Tech. Rep. JPL D-66480, Jet Propulsion Lab., California Inst. Technol., Pasadena, CA, USA, Jun. 6, 2018.

[37] T. Bongiovanni *et al.*, "Field observations during the tenth microwave water and energy balance experiment (MicroWEX-10): From Mar. 1, 2011 through Jan. 5, 2012," Center Remote Sensi., Univ. Florida, Gainesville, FL, USA, Tech. Rep., 2015. [Online]. Available: http://edis.ifas.ufl.edu/ae512

[38] T. Bongiovanni *et al.*, "Field observations during the eleventh microwave water and energy balance experiment (MicroWEX-11): From Apr. 25, 2012 through December, 2012," Center Remote Sens., Univ. Florida, Gainesville, FL, USA, Tech. Rep., 2015. [Online]. Available: http://edis.ifas.ufl.edu/ae514

[39] M. Cosh *et al.*, "Estimating vegetation water content during the soil moisture active passive validation experiment," *J. Appl. Remote Sens.*, vol. 13, no. 1, 2019, Art. no. 014516.

[40] INEGI, "Anuario estadístico y geográfico de Tlaxcala 2017," Inst. Nacional De Estadística Y Geografía, México City, Mexico, INEGI, 2017.

[41] M. Jang, K. J. Tien, J. Casanova, and J. Judge, "Measurements of soil surface roughness during the fourth microwave water and energy balance experiment: Apr. 18 through Jun. 13, 2005," Center Remote Sensing, Univ. Florida, Gainesville, FL, USA, Tech. Rep., 2005. [Online]. Available: http://edis.ifas.ufl.edu/AE363

[42] K. Boote, "Data requirements for model evaluation and techniques for sampling crop growth and development," in *DSSAT Version 3.5*, vol. 4, G. Hoogenboom, P. Wilken, and G. Tsuji, Eds. Honolulu, HI, USA: Univ. of Hawaii, 1994, pp. 215–220.

[43] M. Anderson *et al.*, "Upscaling ground observations of vegetation water content, canopy height, and leaf area index during SMEX02 using aircraft and Landsat imagery," *Remote Sens. Environ.*, vol. 92, no. 4, pp. 447–464, 2004.

[44] R. Lira-Colorado, "Manual de usuario. Estaciones climatolicas en Google Earth," Nat. Water Commission Mexico, 2010. [Online]. Available: http://smn.cna.gob.mx/tools/RESOURCES/estacion/EstacionesClimatologicas.pdf

[45] WMO, "Guide to instruments and methods of observation," World Meteorological Org., Geneva, Switzerland, 2018.

[46] G. Mountrakis, J. Im, and C. Ogole, "Support vector machines in remote sensing: A review," *ISPRS J. Photogramm. Remote Sens.*, vol. 66, no. 3, pp. 247–259, 2011.

[47] M. Chaubell *et al.*, "Improved SMAP dual-channel algorithm for the retrieval of soil moisture," *IEEE Trans. Geosci. Remote Sens.*, vol. 58, no. 6, pp. 3894–3905, Jun. 2020.

[48] J. Adams, H. McNairn, A. Berg, and C. Champagne, "Evaluation of near-surface soil moisture data from an AAFC monitoring network in Manitoba, Canada: Implications for L-band satellite validation," *J. Hydrol.*, vol. 521, pp. 582–592, 2015.

[49] G. Voronoï, "Nouvelles applications des paramètres continus á la théorie des formes quadratiques. Deuxième mémoire. Recherches sur les parallélloèdres primitifs.," *J. Die Reine Angewandte Mathematik*, vol. 134, pp. 198–287, 1908. [Online]. Available: http://eudml.org/doc/149291

[50] J. R. Wang and B. J. Choudhury, "Remote sensing of soil moisture content over bare field at 1.4GHz frequency," *J. Geophysical Res.*, vol. 86, no. C6, pp. 5277–5282, 1981.

[51] A. Van de Griend and J. Wigneron, "The b-factor as a function of frequency and canopy type at H-polarization," *IEEE Trans. Geosci. Remote Sens.*, vol. 42, no. 4, pp. 786–794, Apr. 2004.

[52] P. O'Neill, A. Joseph, P. Srivastava, M. Cosh, and R. Lang, "Seasonal parameterizations of the tau-omega model using the ComRAD ground-based SMAP simulator," in *Proc. IEEE Int. Geosci. and Remote Sens. Symp.*, 2014, pp. 2423–2426.

[53] Comisión Nacional del Agua, "Perspectiva de porcentaje de precipitación respecto a la media por Estadio," 2018. [Online]. Available: https://smn.conagua.gob.mx/es/climatologia/pronostico-climatico/precipitacion-form

[54] A. Monsivais-Huertero and J. Judge, "Comparison of bacscattering models at L-band for growing corn," *IEEE Geosci. Remote Sens. Lett.*, vol. 8, no. 1, pp. 24–28, Jan. 2011.

[55] A. Monsivais-Huertero, P. Liu, and J. Judge, "Phenology-based backscattering model for corn at L-band," *IEEE Trans. Geosci. Remote Sens.*, vol. 56, no. 9, pp. 4989–5005, Sep. 2018.

[56] B. Hornbuckle, V. Walker, B. Eichinger, V. Wallace, and E. Yildirim, "Soil surface roughness observed during SMAPVEX16-IA and its potential consequences for SMOS and SMAP," in *Proc. IEEE Int. Geosci. Remote Sens. Symp.*, 2017, pp. 2027–2030.

[57] P. Vermunt *et al.*, "Response of subdaily L-band backscatter to internal and surface canopy water dynamics," *IEEE Trans. Geosci. Remote Sens.*, vol. 59, no. 9, pp. 7322–7337, 2021.

[58] M. A. Inzunza-Ibarra, M. M. Villa-Castorena, E. A. Catalán-Valencia, R. López-López, and E. Sifuentes-Ibarra, "Rendimiento de grano de maiz en deficit hidrico en el suelo en dos etapas de crecimiento," *Revista Fitotecnia Mexicana*, vol. 41, no. 3, pp. 283–290, 2018.
[59] V. Mironov, L. Kosolapova, and S. Fomin, "Physically and mineralogically based spectroscopic dielectric model for moist soils," *IEEE Trans. Geosci. Remote Sens.*, vol. 47, no. 7, pp. 2059–2070, Apr. 2009.
[60] "Conjunto de datos de Perfiles de suelos," Inst. Nacional de Estadística y Geografía, México City, Mexico, Escala 1:250 000, Serie II (Continuo Nacional). [Online]. Available: https://www.inegi.org.mx/temas/edafologia/
[61] "Suelos de la República Argentina 1:500.000," Inst. Nacionalde Tecnologa Agropecuaria, Argentina. [Online]. Available: http://www.geointa.inta.gob.ar/descargas/
[62] H. G. Santos dos *et al.*, "O novo mapa de solos do Brasil: Legenda atualizada," Embrapa Solos-Documentos (INFOTECA-E), Embrapa Solos, Rio de Janeiro, Brazil, Tech. Rep. 130, 2011.
[63] X. Li *et al.*, "Global-scale assessment and inter-comparison of recently developed/reprocessed microwave satellite vegetation optical depth products," *Remote Sens. Environ.*, vol. 253, 2021, Art. no. 112208.
[64] L. Gao, A. Ebtehaj, M. J. Chaubell, M. Sadeghi, X. Li, and J.-P. Wigneron, "Reappraisal of SMAP inversion algorithms for soil moisture and vegetation optical depth," *Remote Sens. Environ.*, vol. 264, 2021, Art. no. 112627.
[65] P. D. Blanco *et al.*, "A land cover map of Latin America and the Caribbean in the framework of the SERENA project," *Remote Sens. Environ.*, vol. 132, pp. 13–31, 2013.
[66] M. Parrens *et al.*, "Global-scale surface roughness effects at L-band as estimated from SMOS observations," *Remote Sens. Environ.*, vol. 181, pp. 122–136, 2016.

Alejandro Monsiváis-Huertero (Senior Member, IEEE) received the B.S. degree in telecommunications engineering from the National Autonomous University of Mexico, Mexico City, Mexico, in 2002 and the M.S. degree in microwaves and optical telecommunications and the Ph.D. degree in microwaves, electromagnetism, and optoelectronics from the University of Toulouse, Toulouse, France, in 2004 and 2007, respectively.

From 2004 to 2006, he was with the Antennes, Dispositifs et Matériaux Microondes Laboratory, and from 2006 to 2007, with the Laboratoire d'Etudes et de Recherche en Imagerie Spatiale et Médicale, both at the University of Toulouse, France. From 2008 to 2009, he was a Postdoctoral Research Associate with the Center for Remote Sensing, Department of Agricultural and Biological Engineering, University of Florida, Gainesville. Since 2010, he has been working as a Researcher with the Escuela Superior de Ingeniería Mecánica y Eléctrica campus Ticoman of the Instituto Politécnico Nacional of Mexico, Mexico City. In 2013, he was as a visiting Researcher with the Centre d'applications et de recherche en télédétection, Département de Géomatique Appliquée, Faculté de Lettres et de Sciences humaines, Université de Shrebrooke, Canada. His research areas of interest include microwave and millimeter-wave radar remote sensing, electromagnetic wave propagation, and retrieval algorithms.

Daniel Enrique Constantino-Recillas (Student Member, IEEE) received the B.S. degree in aeronautical engineering and the M.S. degree in aeronautical and space engineering in 2017 and 2018, respectively, from the Instituto Politécnico Nacional (IPN), Mexico City, Mexico, where he is currently working toward the Ph.D. degree in telecommunications engineering.

From 2015 to 2021, he participated in the Laboratorio de Investigación y Aplicaciones en Percepción Remota Espacial, IPN, where he collaborated in THEXMEX field campaigns in different ecosystems in Mexico. His research interests include microwave electromagnetic models and the implementation of satellite remote sensing methodologies for the monitoring of ecosystems with optical and microwave sensors.

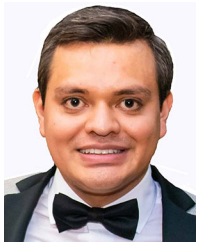

Juan Carlos Hernández-Sánchez (Student Member, IEEE) received the B.S. degree in aeronautical engineering, the M.Eng. degree in aeronautical maintenance, and the M.S. degree in aeronautical and space engineering in 2015, 2016, and 2018, respectively, from the Instituto Politécnico Nacional (IPN), Mexico City, Mexico, where he is currently working toward the Ph.D. degree in telecommunications engineering.

From 2012 to 2021, he participated in the Laboratorio de Investigación y Aplicaciones en Percepción Remota Espacial, IPN. He was working on satellite optical products applying techniques to estimate air pollutants when he studied to obtain his first master's degree. Later, he focused on downscaling SMAP observations in the biosphere reserve of Calakmul in the Southern Mexico. He was a volunteer of SMAPVEX16 in Iowa during the second IOP. He has been working with the Center of Remote Sensing, University of Florida, Gainesville, FL, USA. His main research interests include remote sensing, soil moisture, and enhancing techniques of spatial resolutions.

Héctor Ernesto Huerta-Bátiz (Student Member, IEEE) received the B.S. degree in aeronautical engineering in 2016 from the Instituto Politécnico Nacional (IPN), Mexico City, Mexico, where he is currently working toward the M.Sc. degree in aeronautical and space engineering.

Since 2017, he has been a Career Instructor as an aviation maintenance technician and aeronautical operations officer licensed to teach air law, aerodynamics, air navigation, and digital and analog techniques. He is also a member of the Remote Sensing Research and Applications Laboratory, where he works on the assimilation of satellite data and calibration of soil-vegetation-atmosphere transfer energy models. His areas of interest are those related to remote sensing and control, seeking direct applications in the generation of value for the farmer.

Jasmeet Judge (Senior Member, IEEE) received the Ph.D. degree in electrical engineering and atmospheric, oceanic, and space sciences from the University of Michigan, Ann Arbor, MI, USA, in 1999.

She is currently a Professor in agricultural and biological engineering, Institute of Food and Agricultural Sciences, University of Florida, Gainesville, FL, USA, where she is also the Director of the Center for Remote Sensing. Her research interests include microwave remote-sensing applications to terrestrial hydrology for dynamic vegetation, AI-based spatio-temporal scaling of remotely sensed observations in heterogeneous landscapes, modeling of energy and moisture interactions at the land surface and in the vadose zone, and data assimilation.

Pedro Alejandro López-Estrada received the B.S. degree in computer systems from the Instituto Politécnico Nacional (IPN), Mexico City, Mexico, in 2020.

He is a collaborator of the Laboratorio de Investigación y Aplicaciones en Percepción Remota Espacial, IPN. He currently develops web applications in Python and/or Java. He is a fan of Python and its ecosystem for scientific computing. His areas of interest are cryptography and machine learning, as well as the analysis of georeferenced data for various purposes.

José Carlos Jiménez-Escalona received the M.Sc. in physics of the atmosphere in 2000 and the Doctor of Science degree in physics of the atmosphere in 2005, both from the National Autonomous University of Mexico, Mexico City, Mexico.

He was an Aeronautical Engineer with the National Polytechnic Institute, Mexico City, in 1998. He is currently a Professor-Researcher with ESIME Ticoman of the National Polytechnic Institute, Mexico City. His research interests include the use of satellite images for the monitoring of natural phenomena and their applications to risk mitigation in society.

Eduardo Arizmendi-Vasconcelos received the B.S. degree in aeronautical engineering from the Instituto Politécnico Nacional (IPN), Mexico City, Mexico, in 2017.

From 2015 to 2020, he was with the Laboratorio de Investigación y Aplicaciones en Percepción Remota Espacial, IPN, where he collaborated in THEXMEX field campaigns in Huamantla, Tlaxcala. His area of research is the application of classification algorithms with satellite images.

Marco Antonio García-Bernal received the B.S. degree in aeronautical engineering, the M.S. degree in metallurgical engineering, and the Ph.D. degree in metallurgy and materials from the Instituto Politécnico Nacional (IPN), Mexico City, Mexico, in 2001, 2005 and 2009, respectively.

He has been with the Laboratorio de Investigación y Aplicaciones en Percepción Remota Espacial, IPN, where he has been collaborating in the sample processing of THEXMEX field campaigns. His interests are the mechanical behavior of materials at high temperatures, plastic deformation of metals, FSW/FSP, and light alloy technology for aerospace use.

Cira Francisca Zambrano-Gallardo received the B.S. degree in physics from the Central University of Venezuela, Caracas, Venezuela, in 1998 and the M.I. degree in electrical engineering from the Universidad Nacional Autónoma de México, Mexico City, Mexico, in 2004. She is currently working toward the Ph.D. degree.

From 2004 to 2007, she developed her doctoral studies in image classification for fusion. Since 2019, she has been working as a Professor with the Escuela Superior de Ingenieria Mecánica y Eléctrica Campus Ticomán, Instituto Politécnico Nacional of Mexico, Mexico City.

Alejandra Aurelia López-Caloca received the Ph.D. degree from the National Autonomous University of Mexico (UNAM), Mexico City, Mexico, in 2007, in the field of electrical engineering, digital images, and signals discipline.

She is currently a Researcher and a Postgraduate Teacher with CentroGeo, Mexico City. She works in basic and applied research lines related to data fusion, dynamic systems, spatiotemporal analysis, change detection, and digital classifiers using remote sensing data, including optics, SAR, InSAR, and spatial analysis.

Enrique Zempoaltécatl-Ramírez received the B.S. degree in electrical engineering and the M.Eng. degree in aeronautical maintenance from the Instituto Politcnico Nacional (IPN), Mexico City, Mexico, in 2010 and 2015, respectively.

From 2012 to 2021, he was with the Laboratorio de Investigación y Aplicaciones en Percepción Remota Espacial, IPN. He has been working on satellite radar products determining parameters biophysics in the Southern Mexico ecosystem through the exploitation of radar images and robust algorithms. He has been careering in maintenance aviation since 2009, such as aeronautical mechanic, maintenance engineering, technical auditor in quality assurance, and maintenance operations controller. He is currently developing flight data analysis and aviation quality database areas.

Iván Edmundo De la Rosa-Montero received the B.S. degree in aeronautical engineering and the M.S. degree in aeronautical and space engineering from the Instituto Politécnico Nacional (IPN), Mexico City, Mexico, in 2016 and 2020, respectively.

In 2019, he completed a research internship with the Centre d'Applications et de Recherche en tÉlédétection, Département de Géomatique Appliquée, Faculté de Lettres et de Sciences humaines, Université de Shrebrooke, Canada. He is currently a Researcher and a Consultant in data science with *Cuatro Networks*. His research areas focus on the use of deep learning for pattern recognition in optical images and machine learning for fraud prevention.

Roberto Ivan Villalobos-Martínez received the B.S. degree in aeronautical engineering in 2016 from the Instituto Politécnico Nacional (IPN), Mexico City, Mexico, where he is currently working toward the M.C. degree in aeronautical engineering and space with specialization in remote sensing.

From 2010 to 2016, he was with the Aerospace Integration and Testing Laboratory, and from 2017 to 2021, with Space Remote Sensing Applications and Research Laboratory, both at IPN. His research areas of interest are in hyperspectral microwave sensors and nanosatellites, space design, and retrieval algorithms.

Ramón Sidonio Aparicio-García received the Ph.D. degree from the Instituto Politécnico Nacional (IPN), Mexico City, Mexico, in 2017, in the field of advance technologies, working specifically with digital signal processing, electronics and machine learning disciplines.

He is currently a Researcher with the Research and Development Office in the General Emission Direction of Mexico's Central Bank (Banco de México), besides a teacher with IPN. He often works with image processing, data analytics, machine-deep learning, natural language processing and Big Data technologies applied to the development of tools for internal use of the bank, aiming to the improvement of Mexican banknote qualities. As a teacher, he works mainly with machine learning topics.

Carlos Rodolfo Sánchez-Villanueva received the B.S. degree in aeronautical engineering from the Instituto Politécnico Nacional (IPN), Mexico City, Mexico, in 2021.

From 2018 to 2020, he participated in the Laboratorio de Investigación y Aplicaciones en Percepción Remota Espacial, IPN, where he collaborated in THEXMEX field campaigns in Huamantla, Tlaxcala.

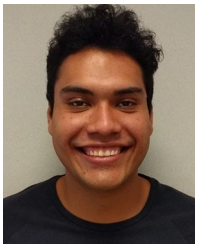

Leonardo Arizmendi-Vasconcelos is currently working toward the Aeronautical Engineering degree with the Instituto Politécnico Nacional (IPN), Mexico City, Mexico.

From 2016 to 2020, he participated in the Laboratorio de Investigación y Aplicaciones en Percepción Remota Espacial, IPN, where he collaborated in THEXMEX field campaigns in Huamantla, Tlaxcala.

Roberto Cotero-Manzo (Student Member, IEEE) received the B.S. degree in physics from the University of Guadalajara, Guadalajara, Mexico, in 2018. He is currently working toward the master's degree with the Instituto Politécnico Nacional (IPN), Mexico City, Mexico, majoring in a space and aeronautics degree with a focus on remote sensing with applications in crop analysis.

Since 2020, he has been a member of the Laboratorio de Investigación y Aplicaciones en Percepción Remota Espacial, IPN, where he collaborated in the THEXMEX field campaigns.

Jaime Hugo Puebla-Lomas received the degree in communications and electronics engineering from the Escuela Superior de Ingenieria Mecanica y Eléctrica Unidad Zacatenco, Instituto Politécnico Nacional (IPN), Mexico City, Mexico, in 1997, and the master's degree in telecommunications engineering from the Graduate Studies and Research Section of the Zacatenco Unit of the National Polytechnic Institute, Mexico City, in 2010.

He participated in the project for the installation of a satellite teleport operating in "C" band with automatic satellite tracking for the Secretary of National Defense, Communications Center of the Military School of Transmissions in Mexico City.

Víctor Manuel Saúce-Rangel received the B.S. degree in metallurgy and materials engineering, in 1984 and the master's degree in metallurgy and materials, in 1992 from the ESIQIE of the Instituto Politécnico Nacional, Mexico City, Mexico, in 1992.

Since 1992, he has been a Professor with ESIME UPT and the Head of the Materials Engineering Laboratory. He has been participating in research activities, thesis management and consulting, industrial and consulting, failure analysis in materials in the metal-mechanical and aeronautical industry, dissemination of results in meetings, congresses and magazines, and also participating in different research projects as the Director and Participant, current friction welding and reverse engineering, composites materials, corrosion, as well as solutions through the group of research in advanced composites materials. His research areas of interest are materials engineering, failure analysis, friction welding, corrosion and reverse engineering